Levitating a Milligram Gravity Source

Seldenthuis, Lars

Levitating a Milligram Gravity Source

THESIS

submitted in partial fulfillment of the
requirements for the degree of

BACHELOR OF SCIENCE
in
PHYSICS

Author :	Lars Seldenthuis
Student ID :	s2897024
Supervisor :	Prof. dr. ir. Tjerk H. Oosterkamp
	Dennis Uitenbroek MSc
Second corrector :	Dr. Wolfgang Löffler

Leiden, The Netherlands, January 28, 2024

Levitating a Milligram Gravity Source

Lars Seldenthuis

Huygens-Kamerlingh Onnes Laboratory, Leiden University
P.O. Box 9500, 2300 RA Leiden, The Netherlands

January 28, 2024

Abstract

The unification of general relativity and quantum mechanics has been a persistent challenge in the field of physics. This study introduces a design for a milligram-scale gravity source, termed the Gravity Propeller. When coupled with the Magnetic Zeppelin, a gravity detector of comparable scale, it could potentially enable the measurement of gravitational interactions between two milligram objects. This measurement could provide insights into the unification of general relativity and quantum mechanics. The propeller, composed of two sets of Meissner levitated magnets connected by a stick, is designed to levitate within a type I superconducting trap and rotate to create a variable gravity potential. This research confirms the levitation of the propeller and demonstrates several optimizations, for instance, the minimization of damping. However, the rotation of the propeller is yet to be accomplished.

Contents

Chapter 1

Introduction

Two of the most famous theories discovered in the previous century are quantum mechanics and general relativity. Quantum mechanics is powerful in describing the interaction between particles at the micro scale, but gravity is not included in this theory yet. The theory of general relativity does have a description of gravity, however only for macroscopic objects.

To solve this problem, the two theories should be combined, however this raises some problems, because they are incompatible. Quantum mechanics is probabilistic whereas the theory of general relativity is deterministic. Also, quantum mechanics speaks of discrete energy levels, whereas energy is continuous in the theory of general relativity.

This problem makes the boundary between the two theories a fascinating area of study. One way to explore this boundary experimentally is by observing quantum effects on a macroscopic object in superposition. Another method is to measure the gravitational interaction between two microscopic objects. This research project will focus on the latter method.

Measuring the gravity of objects in the milligram scale is challenging due to the very small gravitational force the two objects exert on each other, which is in the order of atto newtons. This makes it difficult to detect its effect. To overcome this challenge, mechanical resonators are used to measure the effects of such a small force. When the force acting on the resonator oscillates, many cycles can be used to add energy to the system of the mechanical oscillator. This is especially evident when the frequency of the force matches the resonance frequency of the oscillator, causing its oscillation amplitude to grow to a maximum. Using a mechanical resonator with little damping and thus a high Q factor, the effects due to gravitational coupling between two milligram objects can get into a measurable regime.

To achieve a high Q factor, Meissner levitated magnets inside a superconducting trap are used as mechanical resonators, which ensure minimal damping and thus high Q factors. The oscillation of these magnets can be measured using coils and/or a SQUID. This method has been used to build a milligram gravity detector in the Oosterkamp group, known as the Magnetic Zeppelin [1].

This detector was able to measure the gravity interaction between the Magnetic Zeppelin and the rotating mass wheel, which still weighed in the order of kilograms. The oscillating gravitational force exerted on the Magnetic Zeppelin due to the rotation of the wheel was measured to be 30 atto newtons [1].

The next phase of this research is to scale down the gravity source to the milligram scale. This will in the future enable the measurement of the gravitational interaction between milligram scale objects, which could lead to a better understanding of how to combine the theory of general relativity with quantum mechanics. The development of the milligram gravity source was the focus of this research project.

This thesis begins with an explanation of the research-specific theory in Chapter 2. Chapter 3 provides a detailed description of the design of the milligram gravity source. Three simulations have been conducted, one of which examines the gravitational force exerted on the Magnetic Zeppelin by the milligram gravity source; these are presented in Chapter 4. Chapter 5 outlines the methodology used to detect the first lift-off of the Meissner levitated milligram gravity source. In this chapter, the results are immediately analyzed and discussed. Chapters 6 and 7 focus on the optimization of the gravity source. Specifically, Chapter 6 aims to increase the Q factor of the resonance modes of the gravity source, while Chapter 7 focuses on decreasing the resonance frequencies. Finally, Chapter 8 provides the general conclusion of the research and recommendations for future research are given.

Chapter 2

Theory

2.1 Superconductivity

This section will provide an overview of the fundamentals of superconductors and present theoretical details that are directly relevant to this research.

2.1.1 What is a superconductor?

The first question to be answered is: what is a superconductor? A superconductor is a special type of material that below a certain temperature, its critical temperature T_c, obeys the following properties [2]:

- *Perfect conductivity*, meaning its electrical resistance drops to zero.
- *Perfect diamagnetism*, which is caused by the expulsion of all magnetic fields in the material, this effect is called the Meissner effect.

Depending on which superconductor gets used, the critical temperature varies. During this research lead, tantalum and aluminum will be used as superconductors, which respectively have a critical temperature of 7.2 K [3], 4.5 K [4] and 1.2 K [5], rounded to one decimal place. The provided critical temperatures are theoretical values, they can vary across different samples. The theoretical value can be seen as an upper bound.

In addition to possessing a unique critical temperature, superconductors also exhibit one or two critical fields, depending on their type. This will be discussed in the following subsection.

2.1.2 Types of superconductors

Superconductors can be divided in two groups, which are called type I and type II:

- Type I superconductors are not able to be in their superconducting state when an applied magnetic field at the location of the superconductor exceeds their critical field H_c. [6]
- Type II superconductors, in contrary to type I, have two critical fields. Below the upper critical field H_{c_2}, the material can get to its superconducting state, however in between the lower H_{c_1} and upper critical field H_{c_2}, magnetic fields can penetrate which leads to flux vortices inside the superconductor. Above the upper critical field the superconductor can not be in its superconducting state. [2]

2.1.3 The Meissner effect and London penetration depth

The Meissner effect is the name of the phenomenon of the expulsion of all magnetic fields inside a superconductor. However, the word *all* in this description is a bit to generalizing, as magnetic fields can actually penetrate the surface of a superconductor where they get exponentially more expelled.

The exponential decay constant is called the London penetration depth λ. During this research a foil of tantalum and lead will be used, this makes it important to know whether the material is thick enough to be able to display the Meissner effect. For this reason the London penetration depths of these materials will be discussed during this subsection.

The London penetration depth is temperature dependent, and is mathematically defined as [2]:

$$\lambda(T) \approx \lambda(0) \left(1 - \left(\frac{T}{T_c}\right)^4\right)^{-\frac{1}{2}} \tag{2.1}$$

Where $\lambda(0)$ is the London penetration depth of the superconductor at a temperature of 0 kelvin, which is given by:

$$\lambda(0) = \sqrt{\frac{m}{\mu_0 n e^2}} \tag{2.2}$$

Where m is the mass of electrons, n the number density of free electrons, e the charge of the electrons and μ_0 the permeability of free space.

For lead and tantalum, $\lambda(0)$ is respectively given by 30.5 nm [7] and 100 nm [8]. Using these values the maximum penetration depth can be determined. For the purpose of these calculations, the upper bounds of the temperatures employed during the experiments will be set at 5 kelvin for lead and 3 kelvin for tantalum. This gives for lead a penetration depth of $\lambda(5K) = 31$ nm and for tantalum $\lambda(3K) = 111.6$ nm.

These penetration depths have to be kept in mind. As it will turn out the used materials are at least a factor of 1000 thicker.

Besides looking at the London penetration depth, it is important to know how superconductors behave when a magnetic field is present, because during this research magnets will be levitated above a superconducting surface. In the following section the interaction between magnets and superconductors will be discussed.

2.2 Meissner levitated magnets

In this section, three topics will be discussed: the levitation height of a magnet above a superconductor, the magnetic field strength of a magnet as a function of distance, and the minimal distance between a magnet and the superconducting surface required to break the superconducting state, referred to as the critical distance. To maintain brevity, the derivations of the formulas will not be included in this thesis. However, for readers interested in understanding these derivations, take a look at the master thesis of Dennis Uitenbroek [9].

2.2.1 Levitation height

To find the levitation height of a magnet above a superconducting surface, the method of image dipoles will be used. This method models the effect of a superconductor on a levitating magnet as a image dipole which is positioned mirrored at the opposing side of the superconducting surface, Figure 2.1 shows a sketch of the situation.

Using this method, the levitation height of a magnet can be derived, the first step is deriving the potential energy experienced by the magnet in the z-direction. This is done in the master thesis of D. Uitenbroek [9] and resulted in the following relation:

$$U_z = \frac{B_r^2 V^2}{64\pi\mu_0 z^3}\left(sin^2(\beta) + 1\right) + mgz \tag{2.3}$$

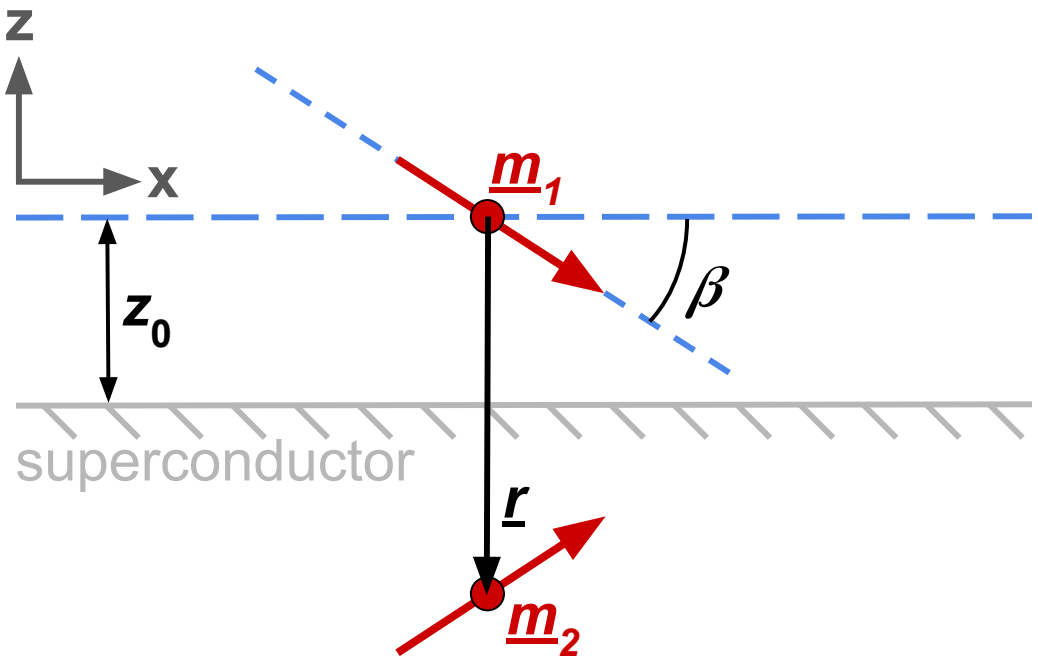

Figure 2.1: *Sketch of the situation, where a magnetic dipole $\mathbf{m}_1$ levitates above a superconducting surface, its magnetization makes an angle β with respect to the surface. At the opposite side of the superconductor the image dipole of $\mathbf{m}_1$ is visible, which is called $\mathbf{m}_2$. The vector connecting the real and image dipole is called $\mathbf{r}$. The levitation height of the real dipole above the superconductor is z_0. Sketch is based on Figure 2.2 of the master thesis of D. Uitenbroek [9].*

The first term of this equation is due to the magnetic interaction between the dipole and the superconductor, the second term is due to gravity. With B_r being the residual magnetic flux density or remanence of the magnet, V the volume of the magnet, m the mass of the whole levitated object, β the angle of the magnetization of the magnet with respect to the superconducting surface, z the distance between the superconductor and the center of the magnet and g being the gravitational acceleration on the surface of the Earth.

Keeping in mind that a system is stable in its lowest energy state, the particle will favour

$$\beta = n\pi \text{ with } n \in \mathbb{N}, \tag{2.4}$$

meaning the magnetic moment will be aligned with the superconducting surface when the particle is stable, resulting in the following potential energy:

$$U_z = \frac{B_r^2 V^2}{64\pi\mu_0} \frac{1}{z^3} + mgz \tag{2.5}$$

To determine the levitation height z_0 where the particle is stable, the minimum of the above expression needs to be found, which can be done by setting its derivative with respect to z to zero and subsequently solving for z:

$$\frac{\partial U_z}{\partial z} = -\frac{3B_r^2V^2}{64\pi\mu_0}\frac{1}{z^4} + mg = 0 \tag{2.6}$$

Solving for z results in the expression of the levitation height z_0 of the magnet as measured from the center of the magnet to the superconducting surface:

$$z_0 = \left(\frac{3B_r^2V^2}{64\pi\mu_0 mg}\right)^{\frac{1}{4}} \tag{2.7}$$

2.2.2 Magnetic field strength

As previously discussed, a superconductor cannot maintain its superconducting state when exposed to a magnetic field with a magnitude exceeding its critical field. This necessitates an understanding of the magnetic field strength of a magnet as a function of distance. The formula for this will not be derived here, as it has already been done by D. Uitenbroek [9]. The derivation assumes that the magnet is spherical and that its magnetization is parallel to the superconducting surface, thus $\beta = 0°$, as this is the preferred state of the magnet as discussed earlier.

Two cases of the magnetic field of a magnet will be examined: the component of the magnetic field parallel to the magnetization and the component perpendicular to the magnetization. Using the convention set in Figure 2.1 with $\beta = 0°$, these correspond to the magnetic field strength in the x- and z-directions, respectively.

In the first case, where the magnetic field points to the x-direction (the same direction as the magnetization), the upper bound of the magnetic field of the magnet is given by [9]:

$$B_x(r) = 2B_r\left(\frac{R_{\text{magnet}}}{r_{\text{surface}}}\right)^3 \tag{2.8}$$

With R_{magnet} being the radius of the magnet, r_{surface} the distance between the center of the magnet and the surface of the superconductor, and B_r the remanence of the magnet.

In the second case, where the magnetic field point to the z-direction (perpendicular to the direction of the magnetization), the expression is given by:

$$B_z(r) = B_r \left(\frac{R_{\text{magnet}}}{r_{\text{surface}}} \right)^3 \tag{2.9}$$

2.2.3 Critical distance

Using the expressions of the magnetic field strength, the minimal distance between the magnet and the superconducting surface to break the superconducting state can be determined, which will be referred to as the critical distance r_{critical}. Rewriting Equations 2.8 and 2.9, results in two equations, one for the x-direction and one for the z-direction:

$$r_{\text{critical, x}} = R_{\text{magnet}} \left(\frac{2B_r}{B_{\text{critical}}} \right)^{\frac{1}{3}} \tag{2.10}$$

$$r_{\text{critical, z}} = R_{\text{magnet}} \left(\frac{B_r}{B_{\text{critical}}} \right)^{\frac{1}{3}} \tag{2.11}$$

In these equations, B_{critical} is the critical field of the superconductor.

2.3 Resonator

In this section the workings of a resonator will be explained, this will aid the understanding of the gravity propeller since it is a mechanical resonator of sorts. Since the design of the propeller will be introduced in Chapter 3, the system can be viewed as a simplified version consisting of just a levitated magnet above a superconducting surface. First, the equation of motion of the magnet in the z-direction will be written down, then the definition of the Q-factor will be covered and finally the damping of the system will be looked into.

2.3.1 Equation of motion in the z-direction

Four types of forces should be considered when writing down the equation of motion: the restoring force due to the magnetic interaction between the magnet and the superconductor, a retarding force due to damping, a constant force due to gravity and finally a magnetic driving force. Later on damping will be covered in more detail, but for now it will be assumed that the retarding force is of the form,

$$F_{\text{retarding, z}} = -\gamma \dot{z} \tag{2.12}$$

The restoring force on the propeller due to the magnetic interaction between the magnet and the superconductor, can be derived using the first term of Equation 2.5, resulting in:

$$F_{\text{restoring, z}} = \frac{3B_r^2V^2}{64\pi\mu_0 z^4} \tag{2.13}$$

In this system a constant force due to gravity is present:

$$F_{\text{constant, z}} = -mg \tag{2.14}$$

Finally, a driving force can be present, which will be discussed in more detail in Chapter 3. For now it can be assumed that it is of the form:

$$F_{\text{driving, z}} = F_0 \sin(\omega t) \tag{2.15}$$

The equation of motion of this system in the z-direction can be derived from the combination of these four forces, resulting in:

$$m\ddot{z} + \gamma\dot{z} - \frac{3B_r^2V^2}{64\pi\mu_0 z^4} + mg = F_0 \sin(\omega t) \tag{2.16}$$

This equation is hard to solve analytically, so later on in Chapter 4, this equation will be solved numerically.

2.3.2 Damping

Despite the efforts to eliminate damping, by performing the experiment at a low temperature and low pressure, the system can still experience mechanical damping. The two main factors of damping will be Eddy current damping and flux trapping.

Eddy current damping

Eddy current damping is a specific type of damping that occurs when a magnet moves in proximity to a conductor. This phenomenon can be explained by Lenz's law, which states that a changing magnetic field will induce a current in a conductor. This induced current will flow in a direction that generates a magnetic field opposing the original one [10]. Consequently, a force is produced that opposes the motion of the magnet. As the induced currents circulate within the conductor, energy is dissipated as heat, thereby damping the mechanical motion of the magnet. This process effectively converts kinetic energy of the magnet into thermal energy and thus damping its motion.

Flux trapping

Another form of damping can be due to flux trapping inside a bulk superconductor, not to be confused with flux pinning in type II superconductors by flux vortices. This theory requires a disclaimer, it has not been proven yet that this really happens but it is something to keep in mind. In this theory a bulk of superconducting material gets modelled as islands of superconductor which are pressed together. When a magnet starts on the surface of the bulk during cooldown, it has penetrating flux lines through the bulk. At the moment the bulk is cooled towards its critical temperature, all islands will one by one become superconducting. Islands will have their own specific moment of becoming superconducting, because of thermal contact and/or impurities in the island. This results in a random order of islands becoming superconducting and thus expelling the magnetic field. In this process flux lines could get trapped between two (or more) of such islands. This process is referred to in this thesis as flux trapping. This effect can occur in both type I and type II superconductors and adds an extra restoring force on the magnet. Figure 2.2 shows an illustration of the process.

2.3.3 Q factor

Using the Q factor, the energy loss of a damped oscillation can be quantified, which is defined by 2π times the energy stored in the oscillator divided by the energy lost in a single period of oscillation [11]. This means that having a high Q factor corresponds to a low energy loss.

At resonance, the Q factor can be related to the decay rate τ of the oscillation, as shown in the following equation:

$$Q = \frac{\tau \omega_{\text{res}}}{2} = \pi f_{\text{res}} \tau \tag{2.17}$$

Where τ is the exponential time constant, ω_{res} is the resonance frequency in radians per second and f_{res} is the resonance frequency in hertz.

2.3.4 Resonance frequencies

The propeller has six degrees of freedom, each corresponding to a unique resonance frequency. While all six resonance modes can be observed, the z-mode, characterized by oscillations in the z-direction, is the only one that can be easily predicted by theory. Therefore, this subsection will focus solely on determining the resonance frequency of the z-mode.

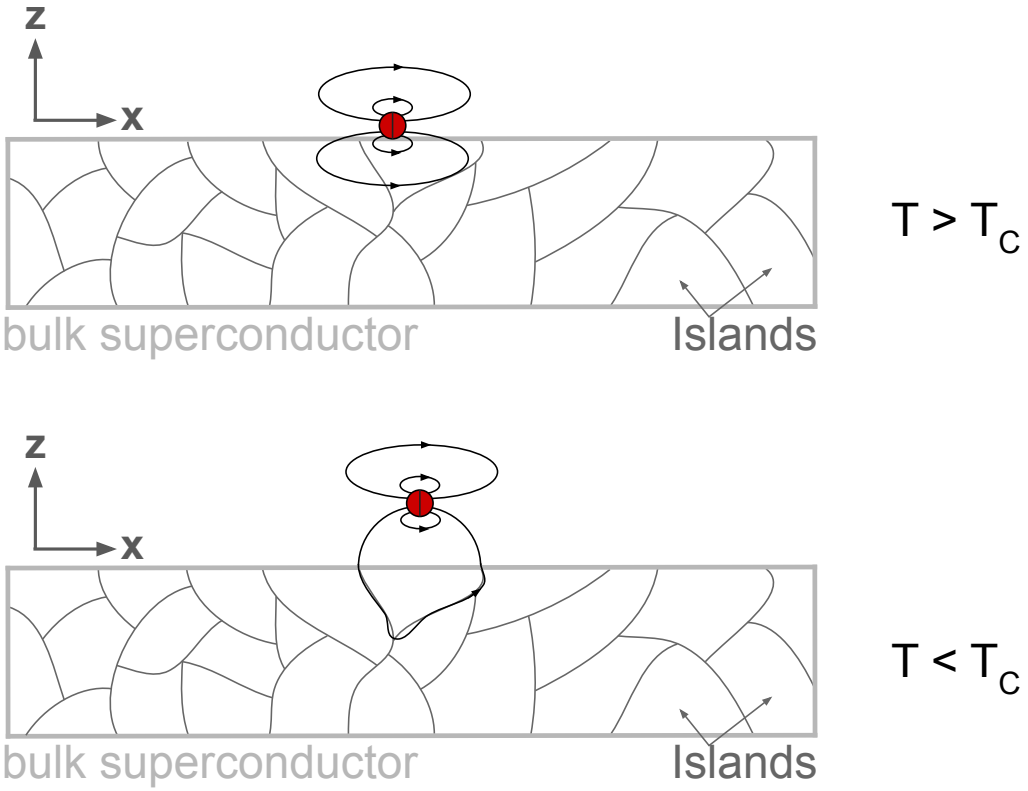

Figure 2.2: *A magnetic dipole rests atop a bulk superconductor composed of islands, with the magnetization of the magnet oriented in the x-direction. Upon transitioning to its superconducting state, the islands repel the magnetic field lines, which subsequently become trapped between the islands.*

Resonance frequency z-mode

The resonance frequency can be determined by first calculating the spring constant. This constant is defined as the second derivative of the potential energy with respect to the variable representing the direction of motion, which in this case is z. Finally, the resonance frequency can be determined by utilizing the relation between the resonance frequency and spring constant, which is defined as:

$$\omega_{\text{res}} = \sqrt{\frac{k}{m}} \tag{2.18}$$

In this equation k is the spring constant and m is the mass of the whole levitated object. To determine the spring constant of the z-mode, the potential

energy as defined in Equation 2.5 will be used, resulting in:

$$k_z = \frac{\partial^2 U_z}{\partial z^2} = \frac{3B_r^2 V^2}{16\pi\mu_0}\frac{1}{z^5} \tag{2.19}$$

This expression of the spring constant can be substituted in Equation 2.18. Finally, by setting z to the levitation height z_0, the resonance frequency of the magnetically levitated object at the levitation height z_0 is found:

$$\omega_{\text{res, z}} = \sqrt{\frac{k}{m}} = \sqrt{\frac{3B_r^2 V^2}{16\pi\mu_0 m}\frac{1}{z_0^5}} \tag{2.20}$$

2.4 Electromotive force

When a magnet moves past a coil, it generates a varying magnetic flux through the surface of the coil. This changing magnetic flux creates an electromotive force (emf) across a normal conducting coil, which can be measured as a voltage. If the coil is assumed to be a fully flattened coil consisting of N windings, the emf can be expressed as:

$$\varepsilon = -N\frac{d\Phi}{dt} \tag{2.21}$$

Where ε is the emf in volts and Φ is the magnetic flux through the coil, which can be defined as:

$$\Phi = \mathbf{B} \cdot \mathbf{S} \tag{2.22}$$

Where $\mathbf{B}$ is the magnetic field and $\mathbf{S}$ is the area vector of the coil. The magnets moving past the coil can be approximated as dipoles, which have the following magnetic field:

$$\mathbf{B}(\mathbf{r}) = \frac{\mu_0}{4\pi}\left[\frac{3\mathbf{r}(\mathbf{m}\cdot\mathbf{r})}{r^5 - \frac{\mathbf{m}}{r^3}}\right] \tag{2.23}$$

Where $\mathbf{r}$ is the position vector and $\mathbf{m}$ is the magnetization of the magnet which is defined by:

$$\mathbf{m} = \frac{\mathbf{B}_r V}{\mu_0} \tag{2.24}$$

With $\mathbf{B}_r$ being the remanence of the magnet and V its volume.

Chapter 3

General design

During this chapter the setup will be discussed, consisting of the design of the propeller, the trap, the drive and detection method of the propeller and finally how everything gets cooled below the critical temperatures of the used superconductors.

3.1 Propeller

As outlined in the introduction, this research aims to develop a milligram scale gravity source. This objective will be accomplished by utilizing levitated magnets positioned above a superconductor. The magnets exhibit minimal damping, thereby reducing the need for active feedback to maintain their steady motion and, consequently, they are able to generate a stable oscillating gravitational potential.

However, if a single magnet were to oscillate to produce a variable gravitational potential, it would create vibrations with each oscillation. This would complicate the task of distinguishing a measured force resulting from gravity from one originating from system vibrations. To mitigate this problem, a solution involving the coupling of two magnets with a stick, referred to as the propeller, will be used. The propeller, through its rotation, can create an oscillating gravitational potential. Furthermore, this design, consisting of a rotating propeller, minimizes additional vibrations. The subsequent section will delve into the design specifics of the propeller.

3.1.1 Fabrication

The propeller is constructed from a wooden cotton swab, which is cylindrical in shape with a diameter of 2.1 mm. Additionally, 6 to 7 NdFeB cube magnets with sides measuring 1 mm and a remanence of 1.4 T, along with GE varnish, are used.

To assemble the propeller, the cotton swab was first cut to a length of 24 mm, resulting in a wooden cylinder with a diameter of 2.1 mm and a length of 24 mm. The stick is then split lengthwise, yielding a halved cylinder. This component of the propeller will be referred to as the stick, and its outline can be seen in Figure 3.1.

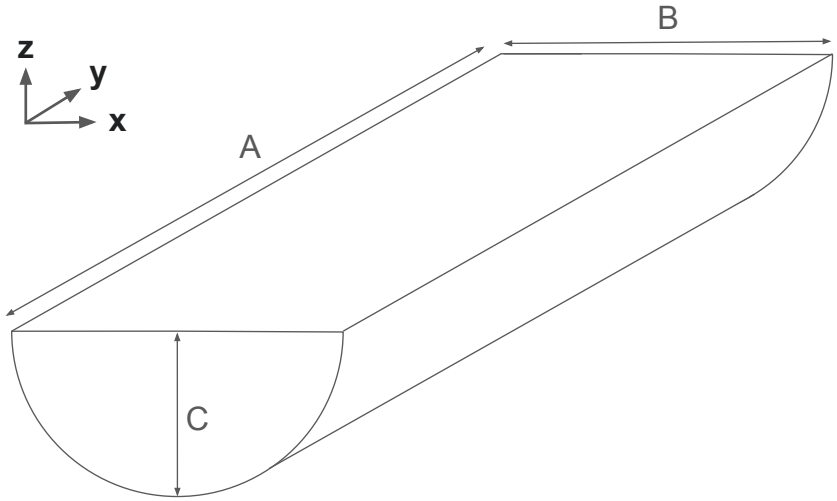

Figure 3.1: *Sketch of the stick of the propeller, which is made of wood and has the shape of a halved cylinder. The indicated sizes are (A) 24 mm, (B) 2.1 mm and (C) 1.05 mm.*

The final step is to glue three magnets to each side of the propeller. Whilst doing this, it is important to keep in mind the magnetization of the magnets. The first group of three magnets has the magnetization pointing perpendicular to the long side of the stick. The other group, at the other end of the stick, has its magnetization pointing in the opposite direction, which is visualized in Figure 3.2.a. The final result is called the propeller, Figure 3.2.b shows a picture of the propeller.

Two propellers are used during the experiments, one with a stick length of 24 mm and three magnets at each side resulting in a total length of 26 mm, which will be called the symmetrical propeller. The other version had

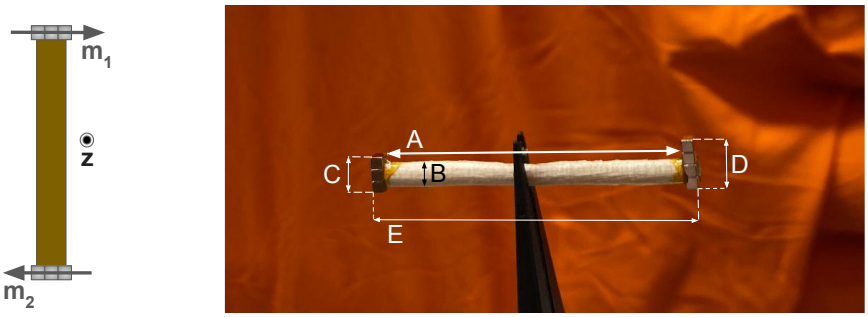

(a) *(b)*

Figure 3.2: *(a): Sketch of top view of propeller, where the direction of the magnetization of the magnets is indicated with arrows (m_1 and m_2). (b): Picture of the propeller being held in the air by a pair of tweezers. This is an asymmetrical propeller with three magnets at one end and four at the other. The indicated sizes are (A) 24 mm, (B) 2.1 mm, (C) 3 mm, (D) 4 mm, (E) 26 mm.*

about the same stick length, but has three magnets at one side and four at the other, which will be called the asymmetrical propeller.

The total mass of the symmetrical propeller is 73.3 mg and the mass of the asymmetrical propeller is 80.9 mg.

3.1.2 Levitation height and critical distance

Using Equation 2.7, the levitation height of the propeller above a superconducting plane can be calculated. The symmetrical propeller has a levitation height of:

$$z_0 = \left(\frac{3 \cdot (1.4\ \mathrm{T})^2 \cdot (6\ \mathrm{mm}^3)^2}{64\pi\mu_0 g \cdot 73.3\ \mathrm{mg}} \right)^{\frac{1}{4}} = 5.84\ \mathrm{mm} \tag{3.1}$$

The asymmetrical propeller will levitate diagonally, where the side with four magnets will levitate a bit higher than the side with three. The mean levitation height of the asymmetrical propeller will be:

$$z_0 = \left(\frac{3 \cdot (1.4\ \mathrm{T})^2 \cdot (7\ \mathrm{mm}^3)^2}{64\pi\mu_0 g \cdot 80.9\ \mathrm{mg}} \right)^{\frac{1}{4}} = 6.16\ \mathrm{mm} \tag{3.2}$$

Using Equations 2.10 and 2.11, the critical distance can be calculated respectively in the x- and z-direction. A critical field value of 80 mT will be used, as this value is approximately accurate for both tantalum [12] and lead [3]. For the group of three magnets, the critical field in the x-direction,

i.e. in the direction parallel to the magnetization of the magnets, is given by:

$$r_{\text{critical, x}} = 1.5 \text{ mm} \cdot \left(\frac{2 \cdot 1.4 \text{ T}}{80 \text{ mT}} \right)^{\frac{1}{3}} = 4.9 \text{ mm} \tag{3.3}$$

In the z-direction, i.e. in the direction perpendicular to the magnetization of the magnets, the critical distance is given by:

$$r_{\text{critical, z}} = 0.5 \text{ mm} \cdot \left(\frac{1.4 \text{ T}}{80 \text{ mT}} \right)^{\frac{1}{3}} = 1.3 \text{ mm}. \tag{3.4}$$

For the group of four magnets, the critical distance in the z-direction is the same as it was for the group of three magnets. However, the critical distance in the x-direction differs:

$$r_{\text{critical, x}} = 2 \text{ mm} \cdot \left(\frac{2 \cdot 1.4 \text{ T}}{80 \text{ mT}} \right)^{\frac{1}{3}} = 6.5 \text{ mm}. \tag{3.5}$$

3.1.3 Resonance modes

The propeller has six resonance modes, each corresponding to a degree of freedom. These modes can be categorized into two types: translation and rotation. The three translation modes correspond to movements in the x-, y-, and z-directions, while the three rotational modes represent rotations around the x-, y-, and z-axes. When discussing the modes of the propeller, its orientation in the coordinate system will assumed to be as illustrated in Figure 3.3.

The purpose of the propeller is to rotate it around the z-axis, creating a varying gravity potential over time. However in order to make it spin, the propeller must first levitate, which will be achieved using a superconducting trap.

3.2 Superconducting trap

As outlined in Chapter 2, the Meissner effect, a characteristic property of superconductors, enables magnets to levitate above their surface. This phenomenon will be used to design the superconducting trap. This trap confines the propeller at its center, where it levitates. It is important to note that, as explained in the theory section, the propeller is oriented such that the magnetization of its magnets is parallel with the superconducting floor of the trap.

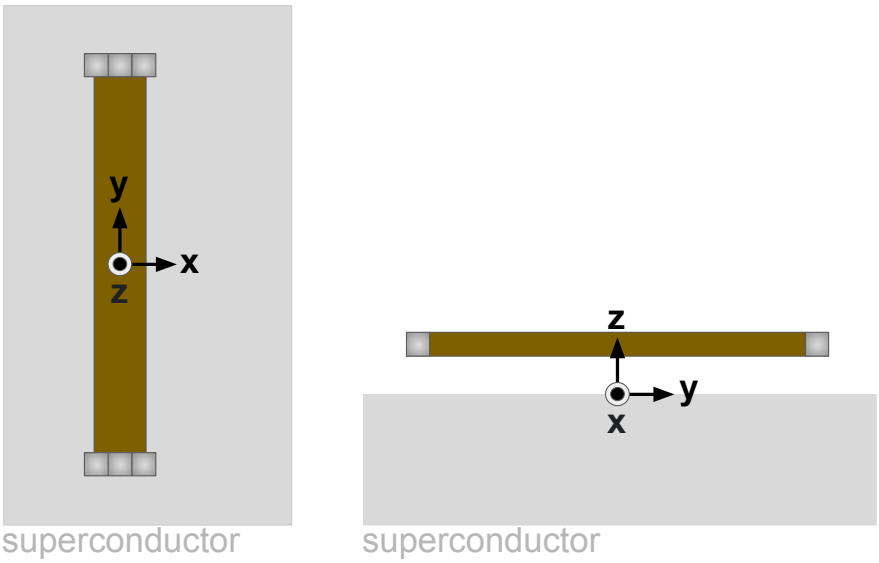

Figure 3.3: *On the left the top view of the propeller levitating above a superconducting plane is shown, on the right side a side view is visible. The orientation of the propeller in this coordinate system will be used to describe its resonance modes.*

3.2.1 Simplified trap

To start, a simplified version of the trap will be shown, later revealed as merely the inner chamber of the full trap. This simplified version resembles a pill box, constructed from a thin film of tantalum measuring 0.1 millimeters in thickness. The box has a diameter of 38 millimeters and a height of 8 millimeters. Its lid has a hole with a diameter of 24 millimeters, to make it easy to feed wires into the box.

A sketch of this simplified trap is presented in Figure 3.4. It should be noted that this simplified version omits certain elements, such as the thermalization strip and the mechanism holding the trap together. These details will be provided during the discussion of the full trap. Additionally, it is important to note that the walls of the trap are also made of tantalum, ensuring that the center of the propeller remains aligned with the center of the trap.

The simplified trap was the starting point of the experiments. However, the propeller did not lift off the floor of the trap when the system was cooled below the critical temperature of tantalum. This issue arose due to the magnets on the surface exceeding the critical field of tantalum. As a result, the tantalum beneath the magnets could not get into its super-

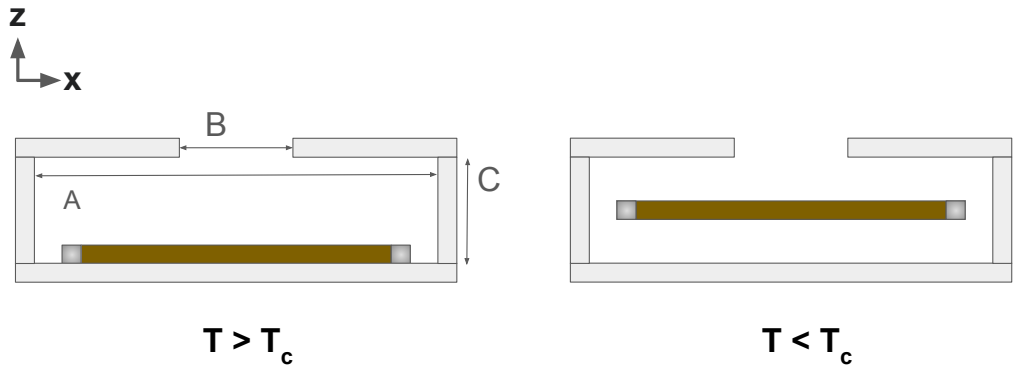

Figure 3.4: *Sketch of the simplified trap, for context the propeller added. The left side shows the starting position of the propeller when the temperature is above the critical temperature of tantalum. On the right side the temperature is below the critical temperature of tantalum causing the propeller to levitate due to the Meissner effect. Using this simplified setup the propeller never levitated although the temperature of the trap was lower than its critical temperature. The size of the trap is: (A) 38.8 mm, (B) 24 mm, (C) 8mm.*

conducting state and, therefore, could not exert a force on the propeller to lift it. The initial thought was that the tantalum parts further than the critical distance of the magnet, which thus would be in their superconducting state, would provide an initial lift of the propeller and subsequently squeeze the magnetic field gradually out off the material until the propeller is fully levitated. However, this expectation was not met. The following section will discuss the full trap, which solves this problem.

3.2.2 Full trap

As previously determined, the critical distance for the magnets of the propeller in the z-direction is 1.3 mm. To enable the propeller to levitate, more superconducting material is added beneath the tantalum. This would position the lower part of the bulk further than the critical distance, allowing a portion of the bulk beneath the propeller to enter its superconducting state and provide the initial lift of the propeller. As the propeller rises slightly, a section of the bulk that initially could not become superconducting due to exceeding of its critical field can now do so. This process will continue until the propeller is fully levitated above the tantalum.

The additional bulk material, approximately 1.5 mm thick, is composed of lead. A 0.3 mm thick copper disk is placed between the lead and the tantalum as a spacer, chosen for its good thermal conductivity. Atop

the copper spacer is a 0.1 mm thick copper disk with four arms, which will be connected to the cryostat to ensure propper thermalization. The trap, which is surrounded by a combination of aluminum and PEEK housing, can be seen in Figure 3.5.

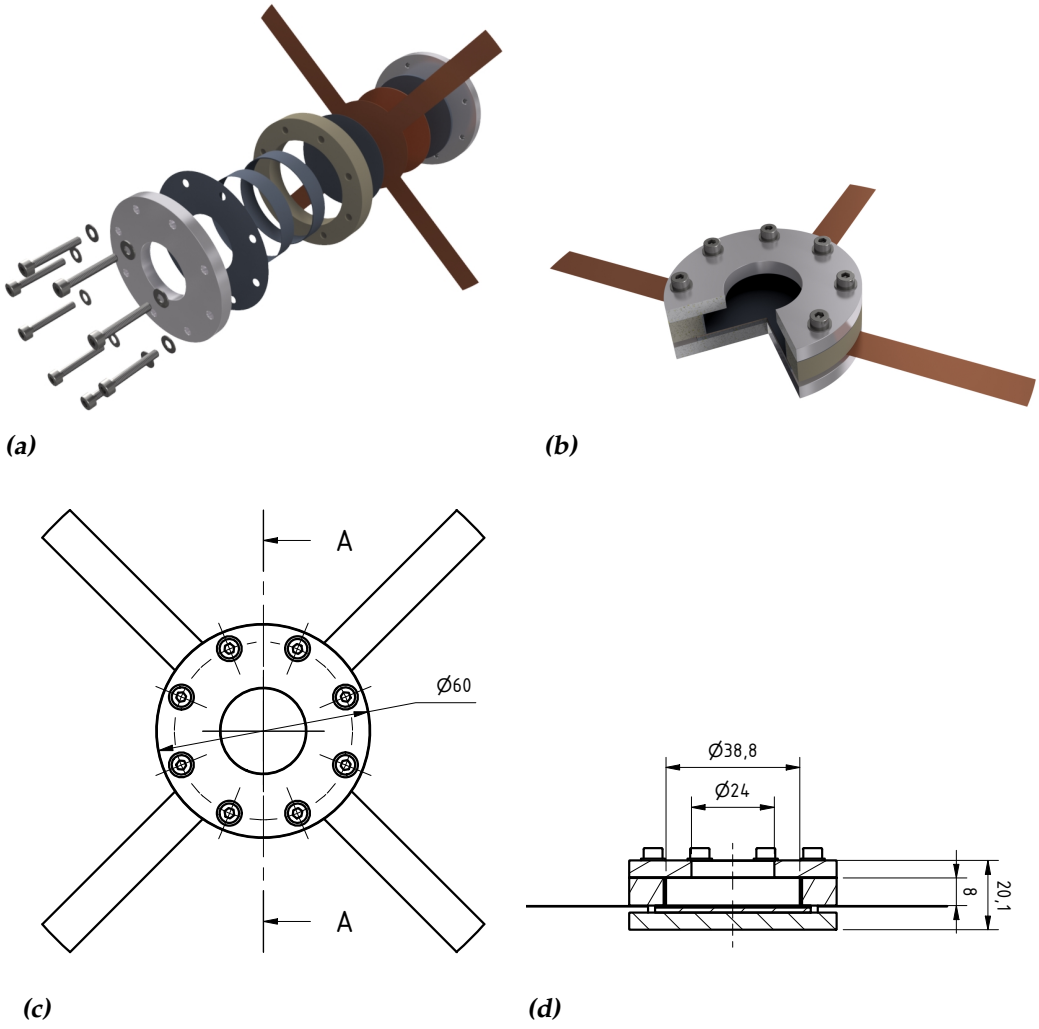

Figure 3.5: *(a) Exploded view of the trap, containing all parts. From right to the left: aluminum bottom plate, lead disk, copper disk, copper disk with four arms for thermalization, tantalum disk, PEEK ring, lead wall, tantalum wall, tantalum disk with hole, aluminum disk with hole, M3 rings, M3 screws. (b) Rendering of the assembled trap, where a pie section is taken away. (c) Sketch of the trap, where the outer radius is indicated in millimeters. (d) Sketch of the cross-section of the trap where the sizes are in millimeters.*

Using the full trap, the propeller is able to levitate. However, at this

moment, there is no way of detecting movement of the propeller or detect if it levitates at all. Also, there is no method to drive the propeller yet. This problem will be solved during the next section.

3.3 Drive and detection

In order to both drive the propeller as detect is motion, coils can be used. As the propeller moves past a coil, it can detect a change in flux due to the movement of the magnets at the end of the propeller. This generates an electromotive force that can be measured using a voltmeter. The coils can also generate a magnetic field, for example an oscillating magnetic field at the resonance frequency of one of the six modes of the propeller.

Four coils are used, made from 80 μm thick copper wire with an external coating. These coils have approximately 30 windings with a diameter of about 5 mm. Due to the fabrication method, the windings are spread over a variable distance of about 1.7 ± 0.3 mm. The coils have an inductance of about 6 μH. The wires leading to and from the coil are twisted to reduce the amount of magnetic field introduced into the cryostat, thereby minimizing noise on other measurements. This twisting also reduces the likelihood of the measuring coil detecting the signal of the driving coil due to crosstalk between their cables.

The coils are attached to the inner wall of the trap using two methods, both of which involve placing a spacer between the coil and the wall. This is because when coils are directly glued to the superconductor, their performance diminishes due to the deflection of nearby magnetic fields by the superconductor, preventing these fields from reaching all parts of the coil. The two methods differ in the material used between the coil and the wall: aluminum or balsa wood.

In the initial setup, the coil was glued to a thin piece of folded aluminum foil, approximately 0.6 mm thick. The coil, with the aluminum behind it, was then glued to the inner wall of the trap, with the aluminum serving as a spacer. This process was repeated for all four coils, allowing for flexibility in measurement and driving at various locations. The coil distribution within the trap can be seen in Figure 3.6.a.

However, using aluminum as a spacer has two drawbacks: it can cause Eddy current damping when not in its superconducting state, and when it becomes superconducting, it can alter the potential energy of the trap, introducing an additional restoring force. This latter can cause the propeller to favor certain positions and influence its ability to rotate around the z-axis. To address this, the aluminum was replaced with a 1 mm thick

piece of balsa wood. The updated version of the trap wall with the coils can be seen in Figure 3.6.b.

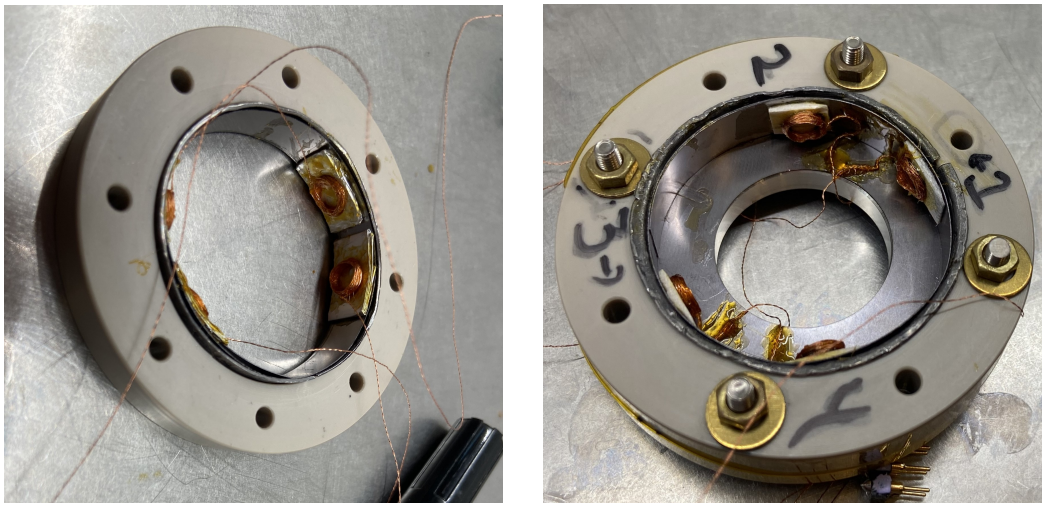

(a) **(b)**

Figure 3.6: *(a) Picture of the middle part of the trap, where the tantalum wall is visible, surrounded by the lead and PEEK ring. The coils are glued to the tantalum wall with a piece of folded aluminum foil in between. (b) In addition to the middle part of the trap, the lid of the trap is also visible in this picture. The coils are glued to the tantalum wall with a piece of balsa wood in between.*

Before the cooldown, the propeller will always be put inside the trap in the same orientation. This orientation can be seen in Figure 3.7. Speaking of cooldown, the final critical part to discuss is cooling the propeller, to get to low enough temperatures such that the lead and tantalum are able to get into their superconducting state.

3.4 Cooling

During the experiments, a dilution fridge is used, which utilizes two cooling methods. These methods cool the cryostat in six temperature zones, ranging from room temperature down to as low as 10 mK.

The first cooling method involves two pulse tubes. Through these, Helium-4 gas is periodically compressed and decompressed at a frequency of 1.4 Hz, resulting in energy extraction from the system. This method can cool the system down to temperatures as low as 3.4 K.

To achieve even lower temperatures, helium-3 and helium-4 gases are mixed in the mixing chamber. This results in an entropy increase in the

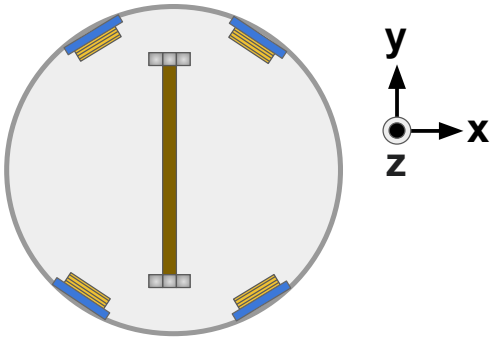

Figure 3.7: *Start position of the propeller before each cooldown. The blue rectangle behind the coils, represents the spacer, which is either made of aluminum or balsa wood.*

gas, which extracts energy from its surroundings. This process enables the lowest temperature zone to reach temperatures as low as 10 mK.

Using the fridge, temperatures below the critical temperature of lead and tantalum can be achieved. Throughout all experiments, the trap was mounted in the lowest temperature zone, on the so called mixing chamber plate, providing the flexibility to utilize the full temperature range of the cryostat.

To ensure proper cooling of the trap, thermal contact must be established. This is crucial because at low temperatures, heat transfer is dominated by phonons. This was achieved by attaching copper strips from the bottom of the trap to the surface of the mixing chamber plate. A visual representation of the mounted trap can be seen in Figure 3.8.

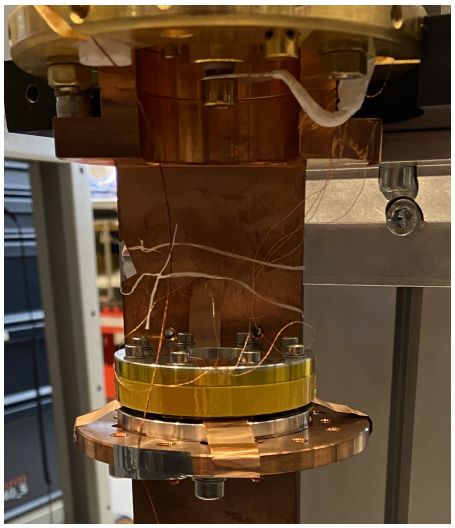

(a)

(b)

Figure 3.8: *(a) Picture of the mounted on the copper shelf, which is connected to the lowest temperature zone of the cryostat. The trap is thermalized using copper strips. (b) Bottom view of the shelf, where the copper strips are visible, which are pressed to the copper shelf using screws to ensure thermal contact.*

Chapter 4

Simulations

4.1 Generated emf due to rotation

The purpose of the propeller is to create an oscillating gravity potential, by rotating it around the z-axis. However, because all experiments will be performed in the cryostat, it is impossible to visually confirm whether the propeller is rotating. This problem is solved by the use of coils. When the propeller moves past a coil it creates an emf which can be measured using a voltmeter. During this section a simulation is made, simulating the created emf due to the rotation of the propeller around the z-axis. In the future, the simulated results can be compared with an actual measured emf, to confirm whether the propeller rotates.

In the simulation, the symmetrical propeller is used inside the simplified trap. One coil with 30 windings and a diameter of 5 mm is placed at the wall of the trap. In the simulation the coil is assumed to be flattened. The magnets at the end of the propeller are treated as magnetic dipoles.

In the starting position, the propeller is aligned with the y-axis, with its center in the origin. The coil is placed on the wall of the trap, with its surface vector pointing towards the outside of the trap. Figure 4.1 shows a sketch of the starting position of the simulation.

The propeller will be simulated to rotate with a frequency of 13.35 Hz, because that an oscillating gravity potential with a frequency of 26.7 Hz will be generated, which is one of the resonance frequencies of the Magnetic Zeppelin [1]. Using the theory introduced in Chapter 2, the emf can be calculated over time. Simulations have been made where the propeller moves clock-wise and counter clock-wise, the results can be viewed in Figure 4.2.

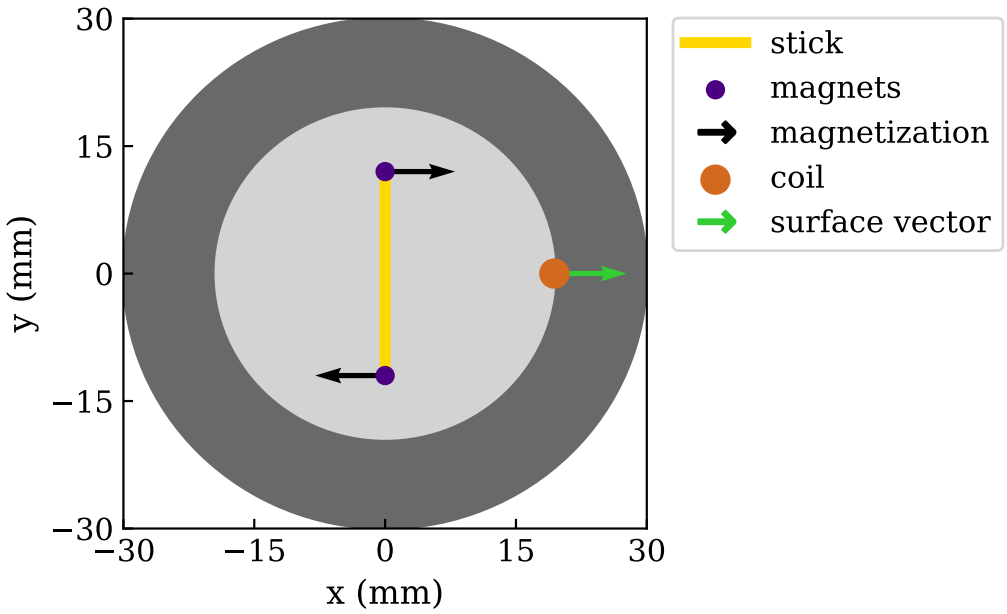

Figure 4.1: *Starting position of the simulation, where the propeller is aligned with the y-axis and its center lies at the origin. A coil is placed at the wall of the trap, with its surface vector pointing towards the outside of the trap.*

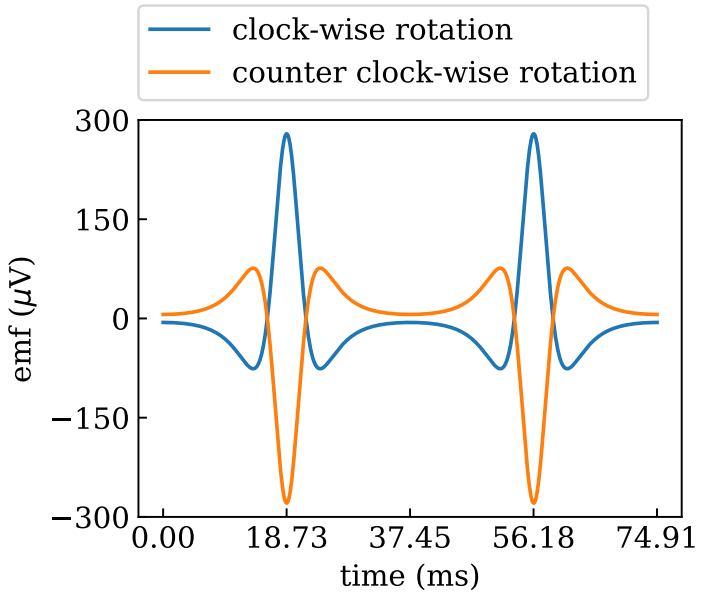

Figure 4.2: *Simulated emf across the coil, when the propeller rotates around the z-axis, with frequency of 13.35 Hz. The propeller has been rotated clock-wise and counter-clockwise. The emf caused by one full rotation of the propeller is plotted.*

4.2 Drop test

Towards the end of the research, the propeller was not able to rotate freely, as will be discussed later. This problem might be caused by an additional restoring force acting on the propeller due to flux trapping. This problem requires a reconsideration of the configuration of the propeller inside trap superconducting trap during the cooldown, especially the moment when lowering the temperature below the critical temperature. A possible solution is locking the propeller to the top of the trap using two coils. Once the trap gets to its superconducting state the coils can be turned off, allowing the propeller to descend into the trap and oscillate towards its equilibrium position. This method could help prevent flux trapping at the bottom of the trap.

For this concept to work, it is crucial to determine whether the downward pointing gravitational force can be overcome by the upward pointing magnetic force acting on the propeller, such that the propeller does not come closer than the critical distance to the bottom of the trap. Otherwise, the bottom of the trap would lose its superconducting state, allowing for flux trapping to occur again.

During this section the problem will be simulated. The symmetrical propeller will be simulated to drop from a height of 7.5 mm above a infinite superconducting plane, where the height is measured from the center of the magnets to the superconducting plane. The drop height corresponds to the height of the propeller if it were to drop from the top of the trap. In the simulation the magnetization of the magnets of the propeller are parallel to the superconducting plane. The equation of motion that needs to be solved is defined by Equation 2.16. In this case there is no driving force, so the equation of motion reduces to:

$$m\ddot{z} + \gamma\dot{z} - \frac{3B_r^2V^2}{64\pi\mu_0 z^4} + mg = 0 \tag{4.1}$$

This equation will be solved numerically, with the start conditions $z(t = 0) = 7.5$ mm and $\dot{z}(t = 0) = 0\,\mathrm{ms}^{-1}$. The damping coefficient is defined as $\gamma = \frac{2}{\tau}$, where a realistic exponential decay time $\tau = 90$ s will be used, as this decay time will be measured in Chapter 6. A plot of the resulting levitation height of the propeller over time, after releasing it from 7.5 mm, can be viewed in Figure 4.3, as well as the Fourier transform of the simulated levitation height.

The simulations show that the propeller will not go below the critical distance and thus not break the superconducting state of the superconductor, when it gets dropped from 7.5 mm above the superconductor

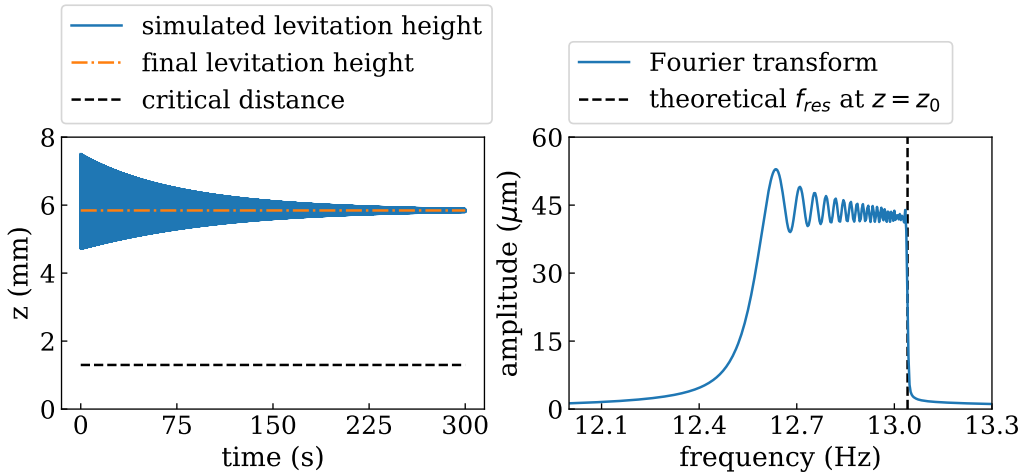

Figure 4.3: *Results of the drop test simulation. On the left side, the simulated levitation height with respect to the center of the magnet is plotted, where the initial 300 seconds after dropping the propeller are shown. On the right, the Fourier transform of the signal as displayed in the left plot is shown, the plot is zoomed-in around the peak due to the oscillation frequency of the propeller.*

with its magnetization parallel to the superconducting plane. The lowest z-position the propeller reaches is about 4.7 mm. Looking at the Fourier transform of the first 300 seconds after dropping the propeller, a frequency shift of the oscillation of the propeller is visible. This shows that the oscillation frequency of the propeller is amplitude dependent. From the Fourier transform can be concluded that when the oscillation of the propeller has a large amplitude its resonance frequency is lower, and when its amplitude dies down it converges towards the theoretical resonance frequency of its final levitation height z_0.

4.3 Gravitational force on the magnetic zeppelin due to the gravity propeller

One of the end goals of the gravity propeller is to measure the varying gravitational potential created by the propeller with the magnetic zeppelin. In this section, a simulation of the rotating gravity propeller will be made, where the gravitational force experienced by the Magnetic Zeppelin will be calculated.

The simulation uses the mass of the full propeller to calculate gravitational force exerted by the propeller on the zeppelin. To accomplish this,

the propeller is divided lengthwise into sections. The total gravitational force is then calculated by summing up the gravitational forces between each section of the propeller and the zeppelin.

The simulation is performed with the symmetrical propeller inside the simplified trap. The center of the propeller is placed at the origin, while the center of the magnetic zeppelin is placed at spatial coordinates (0 mm, 55 mm). Figure 4.4 shows a visual of the setup used in the simulation. The starting position of the propeller is, as indicated in the figure, aligned with the y-axis. The Magnetic Zeppelin has a mass of 0.43 mg [1], for this simulation the zeppelin was treated as a point mass.

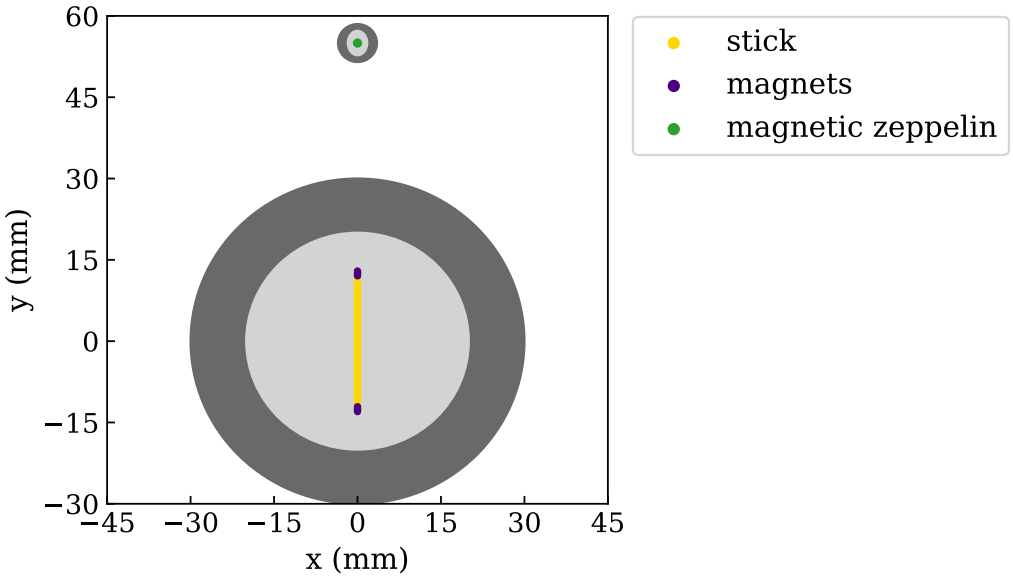

Figure 4.4: *Visualisation of the starting position of the simulation. During the simulation the propeller will rotate around the z-axis. The gravitational force due to the rotation of the propeller will be measured at the location of the magnetic zeppelin.*

During the simulation, the propeller rotates at a frequency of 13.35 Hz because, as mentioned earlier, 26.7 Hz is one of the zeppelin's resonance frequencies [1]. When the propeller rotates at 13.35 Hz, the gravitational potential will oscillate at 26.7 Hz and thus will drive the zeppelin at one of its resonant modes. Figure 4.5 shows the experienced gravitational force by the zeppelin when the propeller rotates clock-wise with a frequency of 13.35 Hz. During the simulation the zeppelin remained in its starting position.

The amplitude of the signal at 26.7 Hz can be determined by taking the

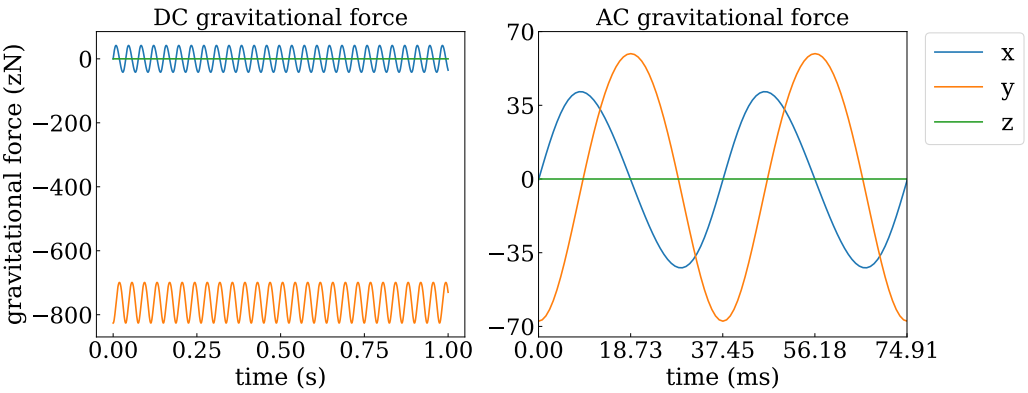

Figure 4.5: *Gravitational force experienced by the magnetic zeppelin due to clock-wise rotation of the gravity propeller with a frequency of 13.35 Hz. Results of the gravity force simulation where the propeller rotates counter clock-wise with a frequency of 13.35 Hz. On the left side the gravitational force including the DC-offset is plotted. On the right side, a plot of the gravitational force due to one full rotation of the propeller is plotted, where the DC-offset is removed, leaving an AC signal.*

Fourier transform of this signal. This way, the amplitude of the gravitational force experienced by the zeppelin in the y-direction is determined to be 63.3 zN.

Based on the simulation, it can be concluded that the gravitational force on the magnetic zeppelin due to the gravity propeller is about 470 times smaller than the gravitational force due to a spinning mass wheel, which was previously used to create a gravitational force with an amplitude of about 30 aN [1]. Options are available to increase the gravitational force by the propeller. For instance, moving the zeppelin closer to a distance of 35 mm off the center of the propeller would result in a gravitational force of about 0.4 aN in the y-direction. At this closer distance, there would be an air gap of 1.5 mm between both traps. For an even higher coupling, the PEEK ring of the trap of the propeller could be made thinner, enabling the zeppelin to move even closer to the propeller and achieve an even higher gravitational coupling.

Chapter 5

First lift-off

This section discusses the method of detection of the first levitated propeller. This method lays the foundation for all other experiments, which will follow the same recipe to achieve results.

The asymmetrical propeller inside the full trap is used, details about this setup have been discussed in Chapter 3. During this experiment, aluminum was between the coil and the wall of the trap. The experiment was conducted at a temperature of about 3 K, causing both lead and tantalum to be in their superconducting state, whilst the aluminum behind the coils was not.

During these experiments the trap was inclined on an angle of about 4.8 degrees, with the slope in the y-direction when looking at Figure 3.7. The end of the propeller with four magnets was positioned at the lower part of the trap. The function of the incline was to ensure that heavier side of the asymmetrical propeller would remain in between the two bottom coils while oscillating and thus not drift away, so that the coils could detect its movement at all times.

Using this setup, the resonance frequency of each resonance mode of the propeller was determined, for some of these modes the Q factor has been measured.

5.1 Frequency sweeps

5.1.1 Method

The first step of finding out whether the propeller levitates or not is by doing a frequency sweep, where one coil creates an oscillating magnetic

field with a gradually increasing frequency, while at the same time another coil measures the emf created due to the motion of the propeller. Using this method six resonance modes should be found, one for each degree of freedom of the propeller.

A lock-in amplifier, the Zurich Instruments HF2LI, is used to both drive and measure signals from the coils. The signal to drive the coil is sent directly from the lock-in to the coil. The signal from the measuring coil first goes to a Stanford Research Systems Model SR560 Low-Noise Preamplifier, which henceforth will be called the pre-amplifier, after the pre-amplifier has amplified the signal by a gain of ten thousand, the signal is measured by the lock-in. The build-in second order lowpass filter of the pre-amplifier was turned on, its cut-off frequency was set to 100 Hz.

When looking at Figure 3.7, the lower two coils were used, where the bottom left coil was used for measuring and the bottom right for driving the propeller.

The frequency sweep was performed in two parts. The first part spanned from 10 Hz to 76.8 Hz, consisting of 807 logarithmically spread frequency points. The second part of the sweep spanned from 85 Hz to 100 Hz and consisted of 105 logarithmically spread frequency points. The sweep function of LabOne of Zurich Instruments automatically chose the integration time and the measurement time of each frequency point. To obtain the final results, the mean of the measured amplitude and phase was calculated at every frequency step, which is used to make amplitude and phase plots as a function of frequency.

5.1.2 Results

The results of the frequency sweep are shown in Figure 5.1. Seven peaks are visible in this plot, where the peaks at 50 Hz and 100 Hz are due to the electrical grid. This leaves six peaks as resonance modes of the propeller. The resonance frequencies for each of these modes can be determined by finding the frequencies at which the amplitude is at a (local) maximum. Errors on these results were defined as half the frequency difference between the peak and a directly neighbouring data point. Using this method, the following resonance frequencies are found: 22.12 ± 0.06 Hz, 26.33 ± 0.07 Hz, 33.84 ± 0.09 Hz, 37.88 ± 0.1 Hz, 41.65 ± 0.1 Hz and 86.97 ± 0.1 Hz.

Looking at the amplitude plot in Figure 5.1, ignoring the resonance peaks, an increase in amplitude with increasing frequency is visible, this is due to the fact that the created emf in the measuring coils scales with the time derivative of the magnetic flux at the location of the coil, $\frac{d\Phi}{dt}$. This ex-

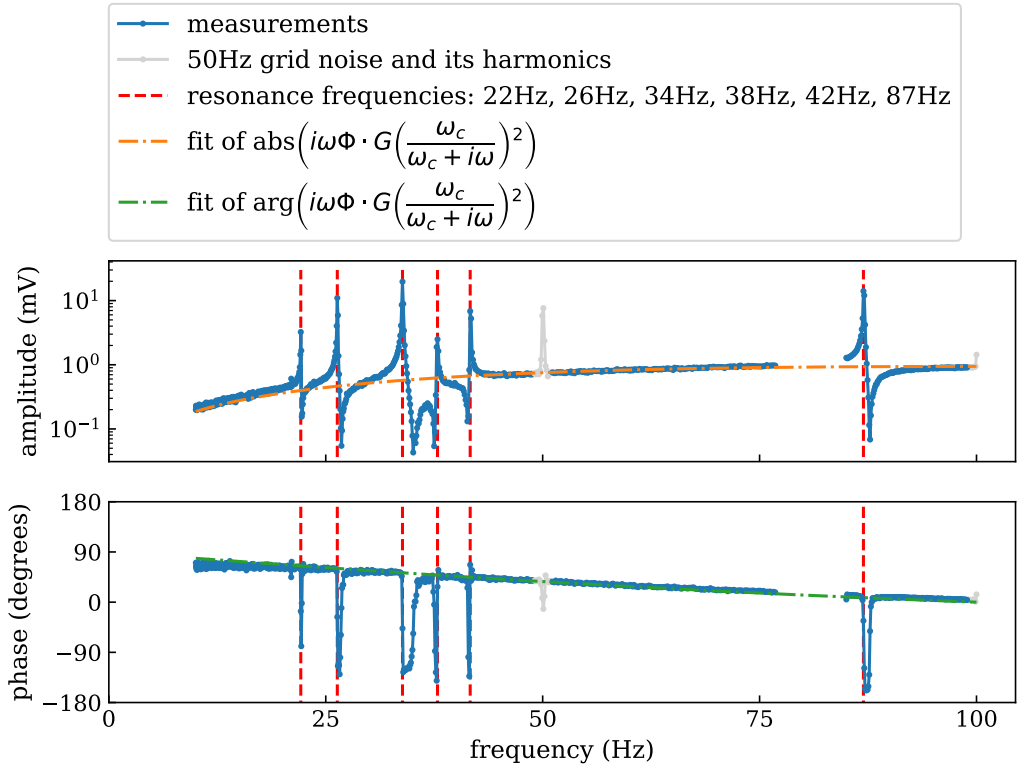

Figure 5.1: *Resulting amplitude and phase plots after the frequency sweep, for the asymmetrical propeller in the full trap on an incline of about 4.8 degrees in the y-direction. Note that the peak at 50 Hz and 100 Hz are due to the power grid and its harmonics, these peaks are shown in gray. The found resonance frequencies are:* 22.12 ± 0.06 *Hz,* 26.33 ± 0.07 *Hz,* 33.84 ± 0.09 *Hz,* 37.9 ± 0.1 *Hz,* 41.7 ± 0.1 *Hz and* 87.0 ± 0.1 *Hz. For both fit functions* G *was set to 10000 and* ω_c *to 100 Hz.* Φ *is used as a fit parameter, which the curve fit method of scipy found to be for the amplitude data* $\Phi = 3 \cdot 10^{-10} \pm 2 \cdot 10^{-24}$*. The found value for* Φ *for the phase data was* $\Phi = 1 \pm 1 \cdot 10^{12}$*.*

pression can be converted to the frequency domain, giving an estimation of the measured voltage:

$$U_{\text{measured}} \sim i\omega\Phi \tag{5.1}$$

This would give a linear increase in amplitude with an increasing frequency. However this is not the complete answer, because a second order low-pass filter was set in series with the circuit with its cut-off frequency set to 100 Hz, which results in an attenuation of the signal. So the measured voltage, including the low-pass filter, can be estimated to be:

$$U_{\text{measured}} \sim i\omega\Phi \cdot \left(\frac{\omega_c}{\omega_c + i\omega}\right)^2 \tag{5.2}$$

This magnitude of this function has been fitted to the amplitude data in Figure 5.1.

For the phase, a fit is made using the assumption that the transfer function scales as U_{measured} as defined in Equation 5.2, so the argument of Equation 5.2 is fitted to the phase data.

5.1.3 Discussion and Conclusion

Using the resonance sweep method, six resonance frequencies were found, one for every degree of freedom of the propeller. It is hard to tell which frequency corresponds to which mode, because no simulations have been performed for this exact configuration. However, this result suggests that the propeller levitates.

It should be noted that the found resonance frequencies of each mode are only valid at the measured amplitude. When the amplitude changes, the resonance frequency of that mode also shifts. This is because the resonance frequencies are dependent on the amplitude of the oscillation, as will be shown in the next section. Furthermore, the frequency sweep was only performed from a low to an increasingly higher frequency, meaning that there is no information about the change of the resonance frequency due to hysteresis.

Figure 5.1 shows after the resonance peaks a decrease in amplitude below the level expected due to mutual induction. This observed decrease in amplitude following the resonance peaks can be attributed to the propeller persisting in its oscillation at the resonance frequency, even after the driving frequency has changed. Meanwhile, the lock-in is emitting a signal at a different frequency. This discrepancy results in the emf produced by the motion of the propeller to be out of phase with the signal transmitted by the lock-in, causing in a reduction of the measured amplitude.

The fits were able to explain the change in amplitude and phase as the frequency increased. However, the used fit function is an approximation of reality, which can explain why the data not always perfectly aligns.

To conclude this section, six resonance frequencies are found, one for each degree of freedom of the propeller. This result suggests that the propeller levitates, because otherwise it would not show six resonance peaks. To further prove this, a damped oscillation of the propeller should be measured after driving it at its resonance frequency. This will further prove

levitation, because a propeller that is not levitated and not driven should just lie on the surface of the trap and thus not show a damped oscillation. This will be shown in the next section by determining the Q factor of the resonance modes by measuring the ringdowns of the oscillations.

5.2 Ringdowns

5.2.1 Method

In order to find the Q factor corresponding to each resonance mode, the propeller is driven on its resonance frequency, which is found using the sweep method. After about ten seconds, the drive gets cut off and using a different coil the emf created by the movement of the propeller will be measured using the lock-in amplifier. During this measurement, an oscillation which exponentially decays is measured. If the measured phase proves to be unstable during this initial ringdown, the resonance frequency of the propeller is just off to the set frequency on the lock-in. To counter this, the frequency of the lock-in gets shifted in accordance such that it does measure on the resonance frequency of the propeller. After this process, the ringdown can be measured and used to determine the Q factor of the resonance mode. The Q factor is determined by calculating the exponential decay time of the oscillation, which as explained in Chapter 2, can be used to calculate the Q factor.

For these measurements the same setup is used as during the previous section. The first ringdown was measured after driving at a frequency of 26.3 Hz, with the three decibel bandwidth of the lock-in set to 486.6 mHz. This measurement will be used as an example for the analysis of the other ringdowns.

5.2.2 Results

The measured ringdown after driving the 26.3 Hz resonance mode is shown in Figure 5.2, where an exponential function has been fitted to the amplitude data and a seventh degree polynomial to the phase data.

From the measured ringdown, the Q factor can be calculated using the exponential decay time that is found by the exponential fit to the amplitude, where the function

$$U(t) = U_0 e^{-t/\tau} \tag{5.3}$$

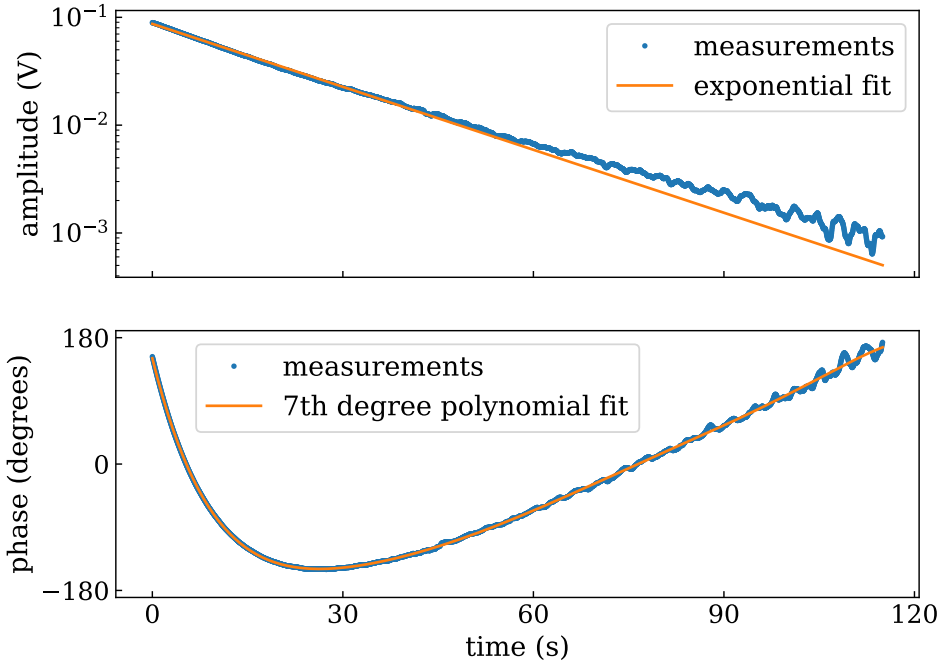

Figure 5.2: *Measured ringdown by the lock-in amplifier, which measured at 26.3 Hz with a 3dB bandwidth of 486.6 mHz. Before the signal of the coil got measured by the lock-in, it was amplified with a gain of ten thousand by the pre-amplifier. The top plot shows the change in amplitude over time of the oscillating propeller, which goes like an exponential function:* $U(t) = U_0 e^{-t/\tau}$*, where the curve fit method of scipy found* $U_0 = 86.95 \pm 0.07$ *mV and* $\tau = 22.31 \pm 0.02$ *s. On the bottom the change in phase of the oscillation over time is showed. For further use of the phase data, a seventh degree polynomial is fitted:* $\phi(t) = at^7 + bt^6 + ct^5 + dt^4 + et^3 + ft^2 + gt + h$*, where the curve fit method of scipy found* $a = (-8.8 \pm 0.3) \cdot 10^{-11}$ *degrees*$/s^7$*,* $b = (4.1 \pm 0.1) \cdot 10^{-8}$ *degrees*$/s^6$*,* $c = (-7.8 \pm 0.2) \cdot 10^{-6}$ *degrees*$/s^5$*,* $d = (8.0 \pm 0.1) \cdot 10^{-4}$ *degrees*$/s^4$*,* $e = (-4.86 \pm 0.06) \cdot 10^{-2}$ *degrees*$/s^3$*,* $f = (1.80 \pm 0.01)$ *degrees*$/s^2$*,* $g = (-3.65 \pm 0.01) \cdot 10^1$ *degrees*$/s$ *and* $h = (1.507 \pm 0.004) \cdot 10^2$ *degrees.*

is fitted to the data. The curve fit method of scipy found $U_0 = 86.95 \pm 0.07$ mV and $\tau = 22.31 \pm 0.02$ s, where the errors are set by the uncertainty in the fit. For the resonance frequency the value as set by the lock-in will be used to calculate the Q factor, where the error is set to its measuring bandwidth, since the actual frequency can have any value within it, so $f_{res} = 26.3 \pm 0.5 Hz$ will be used. Using these parameters, the Q factor can

be calculated for the 26.3 Hz resonance mode, resulting in:

$$\begin{aligned} Q &= \pi f_{res} \tau \\ &= \pi \cdot (26.3 \pm 0.5)\ \text{Hz} \cdot (22.31 \pm 0.02)\ \text{s} \\ &= (18.4 \pm 0.4) \cdot 10^2. \end{aligned} \tag{5.4}$$

Looking at the phase plot of the ringdown in Figure 5.2, it can be concluded that the phase is not constant as the amplitude of the oscillation exponentially decays. This indicates that the resonance frequency is dependent on the amplitude of the oscillation. In order to find the relation of the resonance frequency as a function of the amplitude of the oscillation, a fit to the phase signal as shown in Figure 5.2 will be used. The used fit function is a seventh degree polynomial:

$$\phi(t) = at^7 + bt^6 + ct^5 + dt^4 + et^3 + ft^2 + gt + h \tag{5.5}$$

Where a, b, ..., h are fit parameters, which are determined by the curve fitting routine of scipy and are specified in the caption of Figure 5.2.

The derivative of this function represents the slope at each point of the measured phase signal. To get from this, to the change in frequency Δf that needs to be added to the set lock-in frequency to find the actual resonance frequency over time, the following insight can be used: When a straight line goes through the origin with a slope defined by the derivative of the fit function, than Δf is defined by one over the time it takes for this line to reach a phase value of 360 degrees, i.e.:

$$\Delta f(t) = \frac{\text{slope}}{360} = \frac{1}{360}\frac{d\phi(t)}{dt}. \tag{5.6}$$

Using this definition, Δf can be determined for each data point of the phase data and be added to the resonance frequency to find how the actual resonance frequency changes over time and also, by plotting it against the amplitude, how the resonance frequency is dependent on the amplitude of the oscillation. The results of this process can be seen in Figure 5.3.

To quantify the relation between the resonance frequency as a function of the amplitude, the following function has been fitted the data in the right plot of Figure 5.3:

$$f_{res}(U) = a \cdot U^b + f_0. \tag{5.7}$$

Where a, b and f_0 are the fit parameters that the curve fit method of scipy determined to be $a = -9.29 \pm 0.05 Hz/V^b$, $b = 1.827 \pm 0.002$ and $f_0 = 26.31176 \pm 0.00001$ Hz.

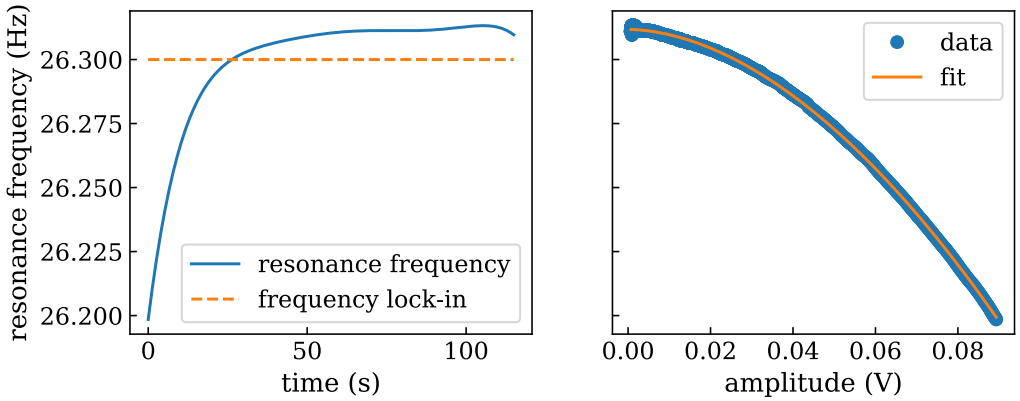

Figure 5.3: *On the left, the resonance frequency as a function of the time is shown, determined using the seventh degree polynomial fit on the phase. On the right, the resonance frequency as a function of the measured amplitude by the lock-in is shown, to which the following function has been fitted:* $f_{res}(U) = a \cdot U^b + f_0$*, where the curve method of scipy found* $a = -9.29 \pm 0.05 Hz/V^b$*,* $b = 1.827 \pm 0.002$ *and* $f_0 = 26.31176 \pm 0.00001$ *Hz.*

To find the Q factor of the 26.3 Hz resonance mode, a series of steps were taken, which can be repeated for the measured ringdowns of other resonance modes. A summary of the found resonance frequencies and Q factors of the six modes can be viewed in Table 5.1. During the measurement of the ringdowns of the 33.3 Hz and 37.5 Hz mode, the bandwidth was set too tight, being 14.49 mHz. This could lead to inaccurate results since the resonance frequency is amplitude dependent, as shown previously. If a frequency shift of approximately 0.1 Hz occurs as before, the frequency would move outside the measurement window. This means that the amplitude will get attenuated, resulting in a less accurate exponential decay time and Q factor.

5.2.3 Discussion and Conclusion

This section showed a method to determine the Q factors of the resonance modes of the propeller. Q factors for three of the six modes are determined: The (26.3 ± 0.5) Hz mode has a Q factor of $(18.4 \pm 0.4) \cdot 10^2$, the (33.30 ± 0.01) Hz mode has a Q factor of 828 ± 1 and finally the (37.50 ± 0.01) Hz mode has a Q factor of 947 ± 1. With the notion that the latter two Q-factors are less accurate due to a too small measuring bandwidth, which could cause the oscillation frequency of the propeller to move outside of the measuring bandwidth of the lock-in and can therefore lead to

SM f_{res}	RDM f_{res}	τ	Q
(22.12 ± 0.03) Hz	x	x	x
(26.33 ± 0.03) Hz	(26.3 ± 0.5) Hz	(22.31 ± 0.02) s	$(18.4 \pm 0.4) \cdot 10^2$
(33.84 ± 0.03) Hz	(33.30 ± 0.01) Hz	(7.91 ± 0.01) s*	828 ± 1*
(37.88 ± 0.03) Hz	(37.50 ± 0.01) Hz	(8.04 ± 0.01) s*	947 ± 1*
(41.65 ± 0.03) Hz	x	x	x
(86.97 ± 0.03) Hz	x	x	x

Table 5.1: *Overview of the resonance frequencies and Q factors of the resonance modes of the propeller. For the calculation of the Q factor of the modes the resonance frequency is used as found by the ringdown method (RDM f_{res}). The asterisks (*) are used to rise awareness that the results were found using a small bandwidth and thus that the results could be inaccurate. The cross (x) indicates that there are no measurements for these modes.*

inaccurate results.

Looking at the amplitude data in Figure 5.2, it can be concluded that the ringdown does not fully seem to follow an exponential function, as the fit does not perfectly align with the data. This could be explained by the fact that at a certain moment noise dominates over the measured emf due to the ringdown, resulting in a deviation of the measured ringdown with respect to an exponential function. This would mean that the actual ringdown of the propeller was exponential, but due to measurement limitations, this could not be perfectly shown.

To conclude this section, only the Q factor of the (26.3 ± 0.5) Hz mode should be taken seriously, which is $Q = (18.4 \pm 0.4) \cdot 10^2$, since the others were measured using a bandwidth that was too small. In future measurements the amplitude dependence of the resonance frequency should be taken into account when setting the bandwidth of the lock-in. Furthermore, the measurement of the ringdowns proves that the propeller levitates, because a propeller that is not levitated and not driven should just lie on the surface of the trap and thus not show a damped oscillation.

Chapter 6

Increasing the Q factor

An important measure of the propeller is damping, because it determines the energy loss of the propeller and therefore the need for active feedback. To keep Eddy current damping as low as possible, aluminium (a normal conductor) is removed from behind the coils inside the trap and exchanged for balsa wood (an insulator). Balsa wood is chosen, because it is an electrically insulating material and will thus not cause Eddy current damping. The change in Q factor will be compared to the previous version of the trap. The experiments were performed at a temperature of about 1.2 K, so the lead and tantalum were superconducting, but the aluminum was not. When the aluminum was exchanged for balsa wood, the propeller was also swapped for the symmetrical propeller, whereas during the first test with the aluminum behind the coils, the asymmetrical propeller was still used. During these tests the trap was not inclined.

6.1 Method

As said earlier, during this experiment the aluminum behind the coils were exchanged for balsa wood. Before and after the exchange, the resonance frequencies of the propeller and their Q factors were determined using the same method as described in the previous chapter.

6.2 Results

The found resonance frequencies for the trap with aluminum and balsa wood behind the coils are shown in Table 6.1, these are determined using

the frequency sweep method and the ringdown method. Table 6.2 shows the measured Q factors. It should be noted that the sweep data was not saved properly, meaning only screenshots of the sweep could be used to determine the resonance frequencies, for that reason a bigger error is given to the resonance frequencies, which is defined as half of the smallest frequency scale visible in the screenshot. This was only the case for the sweep method, since the results of ringdown method were saved properly.

	SM f_{res} Al	RDM f_{res} Al	SM f_{res} Balsa	RDM f_{res} Balsa
Mode 1	(23 ± 1) Hz	(23.3 ± 0.3) Hz	(22.5 ± 0.5) Hz	(22.3 ± 0.1) Hz
Mode 2	(27 ± 1) Hz	(27.2 ± 0.3) Hz	(26.5 ± 0.5) Hz	(26.5 ± 0.1) Hz
Mode 3	(35 ± 1) Hz	(35.2 ± 0.3) Hz	(36.0 ± 0.5) Hz	(35.7 ± 0.1) Hz
Mode 4	(38 ± 1) Hz	(38.3 ± 0.3) Hz	(39.0 ± 0.5) Hz	(38.9 ± 0.1) Hz
Mode 5	x	x	(44.0 ± 0.5) Hz	(44.1 ± 0.1) Hz
Mode 6	(87 ± 1) Hz	(88.1 ± 0.3) Hz	x	x

Table 6.1: *Resonance frequencies measured for two versions of the trap, one with aluminum behind the coils and the other with balsa wood behind the coils. The resonance frequencies have been determined using two methods, the frequency sweep method (SM) and the ringdown method (RDM). The trap was flat on the surface and thus had no slope. The cross (x) indicates that there are no measurements for these modes.*

	τ Al	Q Al	τ Balsa	Q Balsa
Mode 1	(17.57 ± 0.04) s	$(12.7 \pm 0.2) \cdot 10^2$	(97.9 ± 0.1) s	$(68.6 \pm 0.3) \cdot 10^2$
Mode 2	(17.29 ± 0.03) s	$(14.8 \pm 0.2) \cdot 10^2$	(24.4 ± 0.2) s	$(20.3 \pm 0.2) \cdot 10^2$
Mode 3	(11.40 ± 0.01) s	$(12.6 \pm 0.1) \cdot 10^2$	(36.56 ± 0.08) s	$(41.0 \pm 0.2) \cdot 10^2$
Mode 4	(57.5 ± 0.2) s	$(69.2 \pm 0.6) \cdot 10^2$	(93.4 ± 0.2) s	$(11.41 \pm 0.04) \cdot 10^3$
Mode 5	x	x	(97.0 ± 0.4) s	$(13.44 \pm 0.06) \cdot 10^3$
Mode 6	(4.82 ± 0.01) s	1334 ± 5	x	x

Table 6.2: *Measured Q factors for two versions of the trap, one with aluminum behind the coils and the other with balsa wood behind the coils. The Q factors are determined using the resonance frequencies as determined by the ringdown method (RDM). The trap was flat on the surface and thus had no slope. The cross (x) indicates that there are no measurements for these modes.*

6.3 Discussion and Conclusion

When the aluminum was replaced with balsa wood, the system underwent more than one change. In addition to the material change, the asymmetrical propeller was swapped for the symmetrical one. However, since the effects of the additional magnet of the asymmetrical propeller would not significantly alter the results in this situation, it was deemed fair to compare the measurements of both systems.

It can be concluded from the results that exchanging aluminum for balsa wood has no effect on the resonance frequency when the aluminum is still a normal conductor. This aligns with theory, because when aluminum is not in its superconducting state, it only adds an additional damping factor due to Eddy currents. Therefore, when it is exchanged for a material that does not create Eddy currents, a drop in damping will occur, but this will not affect the resonance frequency.

As expected, the Q factor changed. It increased for all six resonance modes, with the smallest increase being a factor of about 1.4 and the biggest a factor of 5.4.

However, just removing the aluminum did not remove all sources of Eddy current damping. There is still Eddy current damping due to the copper coils. In future research, it would be interesting to exchange these coils for superconducting variants to test whether even higher Q factors can be achieved.

Chapter 7

Decreasing resonance frequencies

For the propeller to rotate freely around the z-axis, it is crucial that the resonance frequency of the corresponding resonance mode decreases towards DC. If it remains high, this could suggest the presence of a restoring force that prevents the rotation of the propeller. In this chapter, an experiment will be conducted to investigate whether the resonance decreases when only lead is in its superconducting state. This will involve measuring the resonance frequencies of the propeller when just the lead is superconducting, and comparing these measurements with previously recorded resonance frequencies when both lead and tantalum were superconducting, as described in the previous chapter. The measurements were made using the symmetrical propeller in the full trap, with balsa wood behind the coils. Again, the trap had no incline. The pre-amplifier was set to a second order low-pass filter with a cut-off frequency of 1000 Hz and a gain of ten thousand. The experiment was performed at a temperature of about 5 K, causing only lead to be in its superconducting state.

7.1 Method

The tantalum wall is not fully circular but instead slightly elliptic, with the longest diameter being 38 mm and the shortest 37.5 mm. This slight ellipticity could lead to an additional restoring force in the x- and y-directions, and also in the rotational mode around the z-axis. To test this, the trap was heated to just above the temperature of where the tantalum is not superconducting anymore but the lead still is. This is the case, because the lead wall around the tantalum wall was easier to be molded, so represents a better circle. In this case it would thus be expected that the resonance fre-

quency of the x- and y-mode, and the rotational mode around the z-axis will decrease. Furthermore, because there is no lead present above the tantalum in the lid of the trap, the resonance frequency of the z-mode and the rotational modes around the x- and y-axes will also change. Again, the frequency sweep method is used to find the resonance frequencies of the six modes.

7.2 Results

Figure 7.1 shows the results of the frequency sweep, where all six peaks are visible. However, two peaks around 14 Hz and 15 Hz are close to each other. To verify that they are indeed two separate resonance modes, another analysis method was used: the polar plot. When the amplitude and phase of the signal are plotted in the complex plane, a circle will occur for each resonance peak. In the case of the resonance frequencies around 14 Hz and 15 Hz a big circle (1) with a smaller circle (2) are visible, as seen in Figure 7.1, indicating that both peaks are indeed their own resonance modes. An overview of the found resonance frequencies of the six resonance modes can be viewed in Table 7.1.

	SM f_{res} Pb superconducting	SM f_{res} Pb & Ta superconducting
Mode 1	(14.3 ± 0.5) Hz	(22.5 ± 0.5) Hz
Mode 2	(15.3 ± 0.5) Hz	(26.5 ± 0.5) Hz
Mode 3	(21.4 ± 0.5) Hz	(36.0 ± 0.5) Hz
Mode 4	(26.7 ± 0.5) Hz	(39.0 ± 0.5) Hz
Mode 5	(30.3 ± 0.5) Hz	(44.0 ± 0.5) Hz
Mode 6	(76.9 ± 0.5) Hz	x

Table 7.1: *Measured resonance frequencies using the sweep method. The resonances are determined for two situations, when just the lead is in its superconducting state and when both lead and tantalum are in their superconducting state. The cross (x) indicates that there is no measurement for that mode.*

7.3 Discussion and Conclusion

The data presented in Figure 7.1 shows a decrease in amplitude at certain resonance frequencies. This phenomenon could potentially be attributed to too large frequency steps in the sweep, which may result in missing the

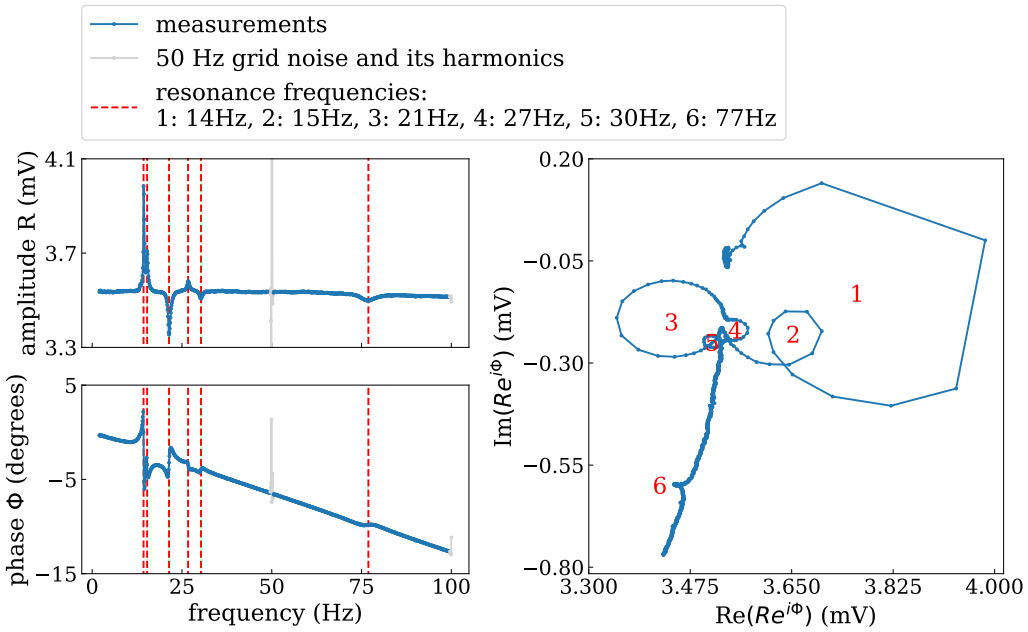

Figure 7.1: *Results of the frequency sweep, where just lead is in its superconducting state. At the top left an amplitude plot is visible, the bottom left shows a phase plot and a polar plot is visible on the right. Each circle in the polar plot represents a resonance peak.*

precise resonance frequency, resulting in measuring the dips after a resonance peak. The dips, also noticeable in Figure 5.1, are potentially due to the propeller maintaining its oscillation at the resonance frequency, even after the driving frequency has shifted. In the meantime, the lock-in is transmitting a signal at a different frequency. This discrepancy causes the emf generated by the motion of the propeller to be out of phase with the signal from the lock-in, leading to a decrease in the measured amplitude. In future research, it would be interesting to test this hypotheses by measuring with a smaller frequency step when this problem occurs.

Looking at the amplitude plot, the about linear increase in amplitude for increasing frequency is not visible as it was in Figure 5.1. During these measurements a different coil was used for measuring the signal. An explanation for not seeing an about linear increase in amplitude could be due to a high resistive connection between the measuring and driving coil in the order of a giga Ohm, which is called a parasitic resistance $R_{\text{parasitic}}$. Using this model, the measured voltage of the system can be estimated as

$$U_{\text{measured}} \sim i\omega\Phi + R_{\text{parasitic}} I \tag{7.1}$$

In this case, the constant term $R_{\text{parasitic}}I$ would dominate over the linear increasing term $i\omega\Phi$ causing the measured amplitude to be about constant.

Furthermore, looking at the phase plot, the phase starts at zero degrees instead of 90 degrees as it did in Figure 5.1. This could be explained using the same reasoning as for the amplitude plot. If the transfer function is estimated to scale with the measured voltage as defined in Equation 7.1, then due to the dominating constant term $R_{\text{parasitic}}I$, the argument will be zero degrees and would barely change as the frequency increases. However, due to the second order low-pass filter, which was set at 1000 Hz, the phase decreases as the frequency increases. So together, the parasitic resistance and the low-pass filter can explain why the phase starts at zero degrees and decreases as the frequency increases.

Comparing the resonance frequencies of only lead in its superconducting state to the resonance frequencies when both lead and tantalum are superconducting, it can be seen that all resonances experienced a frequency drop. This could indicate that the hypothesis is correct and that ellipticity indeed has an influence on the resonance frequencies, as this would explain the frequency drop for the x- and y-mode and the rotational mode around the z-axis. The frequency drop of the z-mode and the rotational mode around the x- and y-axis can be explained by the absence of the restoring force pushing down on the propeller from the top of the trap, since there was no material in its superconducting state as the top had only a layer of tantalum. To verify this result, it would be interesting to make the tantalum wall of the trap as circular as possible and compare if a similar result can be achieved.

During the experiment, the resonance frequencies dropped when only lead was superconducting, compared to when both lead and tantalum were superconducting. However, for the mode that rotates around the z-axis, a further drop approaching DC would be expected. This is because a high resonance frequency for this mode would indicate an additional restoring force that prevents the propeller from rotating freely. A hypothesis for the origin of the additional restoring force is flux trapping, which is explained in detail in Chapter 2. Flux trapping could lead to an increase in the resonance frequency of all six modes. It would be interesting to test this theory by holding the propeller to the top of the trap during cooldown and then dropping it inside when the trap is superconducting. This way, the magnets are further away from the tantalum and lead when it gets superconducting, thus allowing for less flux to be trapped. A simulation for dropping the propeller in the trap is shown in Chapter 4.

Chapter 8

General Conclusion and Outlook

In this research, a milligram gravity source was levitated using the Meissner effect. This was confirmed by measuring six resonance modes of the propeller, each corresponding to a degree of freedom, and by observing the ringdowns of these modes after driving the propeller.

For successful levitation of the propeller, it was critical that the superconductor was thicker than the critical distance of the magnets of the propeller. Otherwise, the propeller would not lift off from the superconducting surface.

Resonance frequencies and Q factors were determined for various iterations of the full trap, with different slopes and materials (aluminum and balsa wood) behind the coils. It was demonstrated that Q factors could be increased by a factor ranging from 1.4 to 5.4, depending on the resonance mode, by replacing aluminum with balsa wood, thereby minimizing Eddy current damping. This suggests that testing superconducting coils in future research could further increase the Q factors.

The resonance frequencies decreased when only lead was superconducting, compared to when both lead and tantalum were superconducting. This could be attributed to the slightly elliptical shape of the tantalum wall, which might have introduced an additional restoring force, compared to the more circular lead wall. Future research could verify this hypothesis by making the tantalum wall as circular as possible and observing if similar resonance frequencies can be achieved as with only lead being superconducting.

Moreover, it was shown that resonance modes of the propeller are amplitude dependent. For future research, it is crucial to measure ringdowns with a sufficiently large bandwidth to accommodate this shift, ensuring that the resonance frequency remains within the measuring domain dur-

ing the ringdown.

During this research, it was not proven that the propeller could rotate around the z-axis. A possible explanation for this could be flux trapping, which might introduce an additional restoring force, preventing the propeller from rotating freely. To test this hypothesis, future research could involve dropping the propeller from the top of the trap and observing whether this causes the resonance frequencies decrease.

Acknowledgements

Dit is het einde van mijn scriptie en wat heb ik veel geleerd tijdens dit onderzoeksproject. Naast veel waardevolle kennis, heeft dit project nogmaals de bevestiging gegeven dat ik experimenteel onderzoek enorm leuk vind! In het bijzonder wil ik Tjerk en Dennis bedanken, jullie stonden altijd klaar om mijn vragen te beantwoorden, dit hielp mij enorm om in korte tijd bekend te worden met alle concepten van dit experiment. Verder wil ik ook de andere leden van de Oosterkamp groep bedanken: Jaimy, Koen en Loek. Ik heb het erg gezellig gevonden om tijdens dit project jullie (beter) te leren kennen en voelde me altijd erg welkom in deze onderzoeksgroep. Daarnaast ook bedankt aan de Hensen groep; Bas en Martijn, waarmee we onze onderzoeksproblemen konden delen tijdens de gravitatie meetings.

De masterstudenten die gelijktijdig hun project deden met mij; João, Richard en Eli, het was altijd erg gezellig om een gesprek met jullie aan te knopen, nog succes met het afronden van jullie projecten!

Tot slot wil ik de FMD en de ELD bedanken voor hun ondersteuning bij dit project, in het bijzonder Merlijn. Hij heeft de 'superconducting trap' gemaakt en voor de prachtige 3D-renderings hiervan gezorgd, die te zien zijn in figuur 3.5.

Bibliography

[1] T. M. Fuchs, D. Uitenbroek, J. Plugge, N. van Halteren, A. Vinante, H. Ulbricht, and T. H. Oosterkamp, "Magnetic zeppelin: Detection of gravitational drive in the hz regime," *arXiv preprint arXiv:2303.03545*, 2023.

[2] M. Tinkham, *Introduction to superconductivity*. Courier Corporation, 2004.

[3] G. Chanin and J. Torre, "Critical-field curve of superconducting lead," *Physical Review B*, vol. 5, no. 11, p. 4357, 1972.

[4] J. Milne, "Superconducting transition temperature of high-purity tantalum metal," *Physical Review*, vol. 122, no. 2, p. 387, 1961.

[5] J. F. Cochran and D. Mapother, "Superconducting transition in aluminum," *Physical Review*, vol. 111, no. 1, p. 132, 1958.

[6] M. Hasan and S. Ali, "Properties and types of superconductors," *Materials Research Foundations*, vol. 132, pp. 17–48, 2022.

[7] R. F. Gasparovic and W. McLean, "Superconducting penetration depth of lead," *Physical Review B*, vol. 2, no. 7, p. 2519, 1970.

[8] T. Greytak and J. Wernick, "The penetration depth in several hard superconductors," *Journal of Physics and Chemistry of Solids*, vol. 25, no. 6, pp. 535–542, 1964.

[9] D. Uitenbroek, "Meissner Levitating Micro Particle," 2021.

[10] Y. Xin, W. Li, Q. Dong, T. Yang, B. Tian, and Q. Li, "Superconductors and lenz's law," *Superconductor Science and Technology*, vol. 33, no. 5, p. 055004, 2020.

[11] G. Fowles and G. Cassiday, *Analytical Mechanics*. Analytical Mechanics, Thomson Brooks/Cole, 2005.

[12] Q. Hu and Z. Wang, "Superconducting characteristics in purified tantalum-foils," *Physica C: Superconductivity and its Applications*, vol. 550, pp. 85–91, 2018.